Spectroscopy of Mixed-Valence Cu_A-Type Centers: Ligand-Field Control of Ground-State Properties Related to Electron Transfer

Daniel R. Gamelin,[†] David W. Randall,[†] Michael T. Hay,[‡] Robert P. Houser,[§] Ton C. Mulder,[⊥] Gerard W. Canters,[∥] Simon de Vries,[⊥] William B. Tolman,[§] Yi Lu,[‡] and Edward I. Solomon*,[†]

Contribution from the Department of Chemistry, Stanford University, Stanford, California 94305, Department of Chemistry, University of Illinois at Urbana−Champaign, Urbana, Illinois 61801, Department of Chemistry and Center for Metals in Biocatalysis, University of Minnesota, Minneapolis, Minnesota 55455, Department of Microbiology and Enzymology, Technical University of Delft, 2628 BC Delft, The Netherlands, and Leiden Institute of Chemistry, Gorlaeus Laboratories, 2300 RA Leiden, The Netherlands

Received September 9, 1997

Abstract: Using a combination of electronic spectroscopies, electronic structural descriptions have been developed for a series of binuclear Cu_A-type centers in *Bacillus subtilis* C*c*O and engineered into the blue copper proteins *Pseudomonas aeruginosa* azurin and *Thiobacillus versutus* amicyanin. Parallel descriptions are developed for two structurally characterized mixed-valence (MV) and homovalent (II,II) synthetic copper thiolate dimers. Assignment of the excited-state spectral features allows the electronic structures of Cu_A and the MV model to be understood and compared in relation to their copper coordination environments. These electronic structural descriptions are supported by SCF-Xα-SW MO calculations, which are used to test systematically the effects of major structural perturbations linking the MV model geometry to that of Cu_A. It is determined that both Cu−Cu compression and removal of the axial ligands are critical determinants of the orbital ground state in these dimers. The weakened axial interactions in Cu_A appear to parallel the mechanism for protein control of electron transfer (ET) function observed in blue copper centers. The major geometric and electronic features of Cu_A, including metal−ligand covalency, redox potentials, reorganization energies, valence delocalization, and the weakened axial bonding interactions, are discussed in relation to its ET function, and specific potential ET pathways are identified and compared.

Introduction

Cytochrome *c* oxidase (C*c*O) is the terminal aerobic respiration enzyme, coupling the catalytic four-electron reduction $O_2 \rightarrow 2H_2O$ to transmembrane proton pumping and long-range electron transfer (ET).[1,2] The catalytic active site is a heme−Cu pair, while a second heme and an additional copper site, Cu_A, serve as ET intermediaries between cytochrome *c* and the catalytic active site. Nitrous oxide reductase (N_2OR) is the terminal denitrification enzyme, reducing N_2O to $N_2 + H_2O$, and is also coupled to long-range ET. Early spectroscopic and biochemical comparisons recognized the presence of a Cu ET site in N_2OR that is very similar to the Cu_A site in C*c*O[3−6] and, in particular, that both involve highly covalent Cu−S(Cys) bonding interactions.[7−11]

Copper thiolate centers are ubiquitous in biological ET. The vast majority of the known Cu−S(Cys) active sites are members of the mononuclear blue-copper family, characterized by their low-energy S(Cys) → Cu charge-transfer (CT) transitions. Although early spectroscopic studies implicated Cu−S(Cys) bonding in the Cu_A site, its EPR and MCD spectroscopies indicated that Cu_A is not a blue copper center.[7−9] The recent confirmation that the Cu_A site is binuclear, containing an extremely short Cu−Cu separation (∼2.44 Å),[12−16] has imparted

[†] Stanford University.
[‡] University of Illinois.
[§] University of Minnesota.
[⊥] Technical University Delft.
[∥] Leiden University.

(1) Babcock, G. T.; Wikström, M. *Nature* **1992**, *356*, 301−307.
(2) Chan, S. I.; Li, P. M. *Biochemistry* **1990**, *29*, 1−12.
(3) Kroneck, P. M. H.; Antholine, W. E.; Riester, J.; Zumft, W. G. *FEBS Lett.* **1988**, *242*, 70−74.
(4) Scott, R. A.; Zumft, W. G.; Coyle, C. L.; Dooley, D. M. *Proc. Natl. Acad. Sci. U.S.A.* **1989**, *86*, 4082−4086.
(5) Antholine, W. E.; Kastrau, D. H. W.; Steffens, G. C. M.; Buse, G.; Zumft, W. G.; Kroneck, P. M. H. *Eur. J. Biochem* **1992**, *209*, 875−881.
(6) Zumft, W. G.; Dreusch, A.; Loechelt, S.; Cuypers, H.; Friedrich, B.; Schneider, B. *Eur. J. Biochem.* **1992**, *208*, 31−40.
(7) Vängård, T. In *Copper Proteins*; Swartz, H. M., Bolton, J. R., Borg, D. C., Eds.; Wiley & Sons: New York, 1972; pp 411−447.
(8) Peisach, J.; Blumberg, W. E. *Arch. Biochim. Biophys.* **1974**, *165*, 691−708.
(9) Greenwood, C.; Hill, B. C.; Barber, D.; Eglinton, D. G.; Thomson, A. J. *Biochem. J.* **1983**, *215*, 303−316.
(10) Hoffman, B. M.; Roberts, J. E.; Swanson, M.; Speck, S. H.; Margoliash, E. *Proc. Natl. Acad. Sci. U.S.A.* **1980**, *77*, 1452−1456.
(11) Stevens, T. H.; Martin, C. T.; Wang, H.; Brudvig, G. W.; Scholes, C. P.; Chan, S. I. *J. Biol. Chem.* **1982**, *257*, 12106−12113.
(12) Blackburn, N. J.; Barr, M. E.; Woodruff, W. H.; van der Oost, J.; de Vries, S. *Biochemistry* **1994**, *33*, 10401−10407.
(13) Blackburn, N. J.; de Vries, S.; Barr, M. E.; Houser, R. P.; Tolman, W. B.; Sanders, D.; Fee, J. A. *J. Am. Chem. Soc.* **1997**, *119*, 6135−6143.
(14) Iwata, S.; Ostermeier, C.; Ludwig, B.; Michel, H. *Nature* **1995**, *376*, 660−669.
(15) Tsukihara, T.; Aoyama, H.; Yamashita, E.; Tomizaki, T.; Yamaguchi, H.; Shinzawa-Itoh, K.; Nakashima, R.; Yaono, R.; Yoshikawa, S. *Science* **1996**, *272*, 1136−1144.
(16) Tsukihara, T.; Aoyama, H.; Yamashita, E.; Tomizaki, T.; Yamaguchi, H.; Shinzawa-Itoh, K.; Nakashima, R.; Yaono, R.; Yoshikawa, S. *Science* **1995**, *269*, 1069−1074.

S0002-7863(97)03161-2 CCC: $15.00
Published on Web 05/15/1998

Chart 1

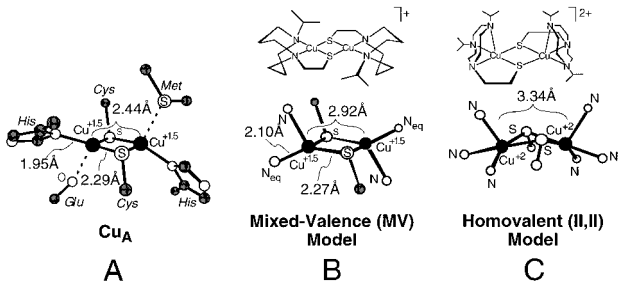

significant momentum toward understanding its unique spectroscopic characteristics.

Previous studies of the Cu_A centers in C*c*O and N_2OR have described the geometric properties of this site. Through a combination of EXAFS,[12,13] X-ray crystallography,[14−16] Raman,[17] and biochemical studies,[18−22] the Cu_A site is now known to be comprised of two Cu ions bridged by two S(Cys) atoms with two N(His) ligands, as illustrated in Chart 1A.[13−16] EPR studies indicate a high degree of similarity between the two Cu ions, implicating a pseudo-inversion center in the dimer. Resonance Raman spectra show enhancement of a large number of core vibrational modes[17,23,24] and indicate that the effective site symmetry of the chromophore is no higher than C_i. Detailed analysis of the vibrational data suggests that the Cu−N(His) bonds are both removed ∼40° from the Cu−Cu axis,[17] while in the crystallographic results, shown in Chart 1A, these angles are ∼10−20°. X-ray crystallographic studies place the axial ligands (one methionine sulfur, S(Met), and one amide oxygen of the glutamate, O(Glu)) between ∼2.2 and 3.0 Å from the Cu ions,[14−16] while there is no evidence for their presence in the EXAFS data.[13]

The Cu_A electronic structure has been studied using complementary theoretical and experimental approaches.[10,11,24−36] ENDOR studies of C*c*O Cu_A[10,11,25−28] show ∼3% and ∼1% spin density on the two different N(His) ligands, yielding a total of ∼4% N(His) character in the HOMO.[28] Paramagnetic NMR studies support this notion of inequivalent His ligands in C*c*O Cu_A.[29,30] ENDOR studies on N_2OR Cu_A suggest ∼4% N(His) character on at least one N(His).[37] Quantitative simulation of the N_2OR Cu_A EPR spectra has led to a description of the half-occupied HOMO orbital as a highly covalent MO having ∼34% total electron density shared between the Cu ions and ∼60% total electron density on the two S(Cys) ligands.[32] S K-edge X-ray absorption experiments on Cu_A[38] from *Bacillus subtilis* C*c*O, which measure this covalency directly, indicate 26 ± 3% total S character in the half-occupied HOMO.[35] In a D_{2h} approximation of the Cu_A site (i.e., NCuSSCuN), a b_{3u} dimer orbital, proposed to be the HOMO, was calculated by UHF−INDO/S to be 36% Cu and 56% S in character.[32] On the basis of these calculations, a D_{2h} MO diagram was proposed which, in particular, provided an explanation for the characteristic twin S→Cu CT features observed in absorption and MCD spectra at ∼20 000 cm^{-1}.[32,34] Similar CNDO calculations predict a low-symmetry HOMO (∼42% Cu, ∼42% S), described as alternating σ^* and π^* Cu−S bonding interactions through the four-membered Cu_2S_2 ring.[33]

A major advance in the study of Cu_A-type centers has been allowed by the isolation and expression of soluble Cu_A domain C*c*O fragments from *B. subtilis*,[38] *Paracoccus denitrificans*,[39] *Thermus thermophilous*,[40] and the Cu_A-containing N_2ORV mutant from *Pseudomonas stutzeri*.[41] These systems permit the study of Cu_A in the absence of the other transition-metal centers found in the holoprotein. A great deal of insight into the geometric and electronic structural properties of the Cu_A motif has also been gained from the construction of model systems. A particularly valuable dithiolate-bridged mixed-valence synthetic dimer (MV, Chart 1B) that closely reproduces the coordination environment, oxidation state, and valence delocalization of the Cu_A site has been crystallographically characterized.[42] As with Cu_A, the observation of a seven-line hyperfine splitting pattern in the EPR spectrum of this model indicates a highly delocalized HOMO wavefunction. Absorption intensity at ∼20 000 cm^{-1}, which is so dominant in Cu_A spectra, has diminished by a factor of 4, however, suggesting significant differences in electronic structure. Cu_A-type centers engineered into proteins containing cupredoxin-like folds also provide a series of perturbed Cu_A sites for systematic study. Two constructs have been engineered into blue copper proteins (azurin[43] and amicyanin[44]), and these reproduce the wild-type

(17) Andrew, C. R.; Fraczkiewicz, R.; Czernuszewicz, R. S.; Lappalainen, P.; Saraste, M.; Sanders-Loehr, J. *J. Am. Chem. Soc.* **1996**, *118*, 10436−10445.
(18) Speno, H.; Taheri, M. R.; Sieburth, D.; Martin, C. T. *J. Biol. Chem.* **1995**, *270*, 25363−25369.
(19) Zickermann, V.; Verkhovsky, M.; Morgan, J.; Wikström, M.; Anemueller, S.; Bill, E.; Steffens, G. C. M.; Ludwig, B. *Eur. J. Biochem.* **1995**, *234*, 686−693.
(20) Zickermann, V.; Wittershagen, A.; Kolbesen, B. O.; Ludwig, B. *Biochemistry* **1997**, *36*, 3232−3236.
(21) Kelly, M.; Lappalainen, P.; Talbo, G.; Haltia, T.; van der Oost, J.; Saraste, M. *J. Biol. Chem.* **1993**, *268*, 16781−16787.
(22) Farrar, J. A.; Lappalainen, P.; Zumft, W. G.; Saraste, M.; Thomson, A. J. *Eur. J. Biochem.* **1995**, *232*, 294−303.
(23) Andrew, C. R.; Lappalainen, P.; Saraste, M.; Hay, M. T.; Lu, Y.; Dennison, C.; Canters, G. W.; Fee, J. A.; Nakamura, N.; Sanders-Loehr, J. *J. Am. Chem. Soc.* **1995**, *117*, 10759−10760.
(24) Andrew, C. R.; Han, J.; de Vries, S.; van der Oost, J.; Averill, B. A.; Loehr, T. M.; Sanders-Loehr, J. *J. Am. Chem. Soc.* **1994**, *116*, 10805−10806.
(25) Martin, C. T.; Scholes, C. P.; Chan, S. I. *J. Biol. Chem.* **1988**, *263*, 8420−8429.
(26) Fan, C.; Bank, J. F.; Dorr, R. G.; Scholes, C. P. *J. Biol. Chem.* **1988**, *263*, 3588−3591.
(27) Hansen, A. P.; Britt, R. D.; Klein, M. P.; Bender, C. J.; Babcock, G. T. *Biochemistry* **1993**, *32*, 13718−13724.
(28) Gurbiel, R. J.; Fann, Y. C.; Surerus, K. K.; Werst, M. M.; Musser, S. M.; Doan, P. E.; Chan, S. I.; Fee, J. A.; Hoffman, B. M. *J. Am. Chem. Soc.* **1993**, *115*, 10888−10894.
(29) Bertini, I.; Bren, K. L.; Clemente, A.; Fee, J. A.; Gray, H. B.; Luchinat, C.; Malmström, B. G.; Richards, J. H.; Sanders, D.; Slutter, C. E. *J. Am. Chem. Soc.* **1996**, *118*, 11658−11659.
(30) Dennison, C.; Berg, A.; Canters, G. W. *Biochemistry* **1997**, *36*, 3262−3269.
(31) Kroneck, P. M. H.; Antholine, W. A.; Riester, J.; Zumft, W. G. *FEBS Lett.* **1989**, *248*, 212−213.
(32) Neese, F.; Zumft, W. G.; Antholine, W. E.; Kroneck, P. M. H. *J. Am. Chem. Soc.* **1996**, *118*, 8692−8699.
(33) Karpefors, M.; Slutter, C. E.; Fee, J. A.; Aasa, R.; Ksellebring, B.; Larsson, S.; Vaenngaard, T. *Biophys. J.* **1996**, *71*, 2823−2829.
(34) Farrar, J. A.; Neese, F.; Lappalainen, P.; Kroneck, P. M. H.; Saraste, M.; Zumft, W. G.; Thomson, A. J. *J. Am. Chem. Soc.* **1996**, *118*, 11501−11514.
(35) Williams, K. R.; Gamelin, D. R.; LaCroix, L. B.; Houser, R. P.; Tolman, W. B.; Mulder, T. C.; de Vries, S.; Hedman, B.; Hodgson, K. O.; Solomon, E. I. *J. Am. Chem. Soc.* **1997**, *119*, 613−614.
(36) Larsson, S.; Kaellebring, B.; Wittung, P.; Malmström, B. G. *Proc. Natl. Acad. Sci. U.S.A.* **1995**, *92*, 7167−7171.
(37) Neese, F.; Kappl, R.; Zumft, W. G.; Hüttermann, J.; Kroneck, P. M. H. *J. Biol. Inorg. Chem.* **1998**, *3*, 53−67.
(38) von Wachenfeldt, C.; de Vries, S.; van der Oost, J. *FEBS Lett.* **1994**, *340*, 109−113.
(39) Lappalainen, P.; Aasa, R.; Malmström, B. G.; Saraste, M. *J. Biol. Chem.* **1993**, *268*, 26416−26421.
(40) Slutter, C. E.; Sanders, D.; Wittung, P.; Malmström, B. G.; Aasa, R.; Richards, J. H.; Gray, H. B.; Fee, J. A. *Biochemistry* **1996**, *35*, 3387−3395.
(41) Zumft, W. G.; Viebrock-Sambale, A.; Braun, C. *Eur. J. Biochem.* **1990**, *192*, 591−599.
(42) Houser, R. P.; Young, V. G., Jr.; Tolman, W. B. *J. Am. Chem. Soc.* **1996**, *118*, 2101−2102.

Cu_A structural and/or spectroscopic features well. A third, engineered into the vacant quinol oxidase cupredoxin-like fold (referred to as PCyoA),[45,46] shows significantly perturbed spectral features that have been interpreted as resulting from partial valence localization due to a strong axial interaction between the O(Glu) and one copper (Cu−O(Glu) ≈ 2.28 Å).[34]

In this study, excited-state spectroscopic techniques are used to compare the bonding characteristics of the Cu_A-type centers from *B. subtilis* C*c*O, azurin, and amicyanin to those of the MV model and a homovalent (II,II) analogue[47] (Chart 1C). The major focus of this study is the comparison of the electronic structure descriptions of these systems in light of the structural perturbations that relate the Cu_A and MV model structures, in particular the weakened axial interactions and Cu−Cu compression. Particular attention is given to understanding the origin of the large differences we find in the HOMO character between these two systems. The deeper understanding of Cu_A bonding gained from this comparison is then applied toward understanding its contributions to ET function.

Experimental Section

Sample Preparation. Samples of the wild-type Cu_A center from *B. subtilis* C*c*O,[38] the engineered Cu_A-type constructs engineered into *Pseudomonas aeruginosa* azurin[43] and *Thiobacillus versutus* amicyanin,[44] and the synthetic mixed-valence ($[(L^{iPrdacoS}Cu)_2]^+$)[42] and homovalent ($[(L^{iPr2tacnS}Cu)_2]^{2+}$)[47] models were prepared as described previously.

Electronic Absorption and MCD Spectroscopies. Low-temperature absorption data were collected on a Cary-17 spectrophotometer using a Janis Research Super Vari-Temp cryogenic dewar mounted in the optical path. MCD measurements were performed on Jasco J500 (UV/vis/NIR, S1 and S20 PMT detection) and J200 (NIR, InSb detection) CD spectropolarimeters with sample compartments modified to accommodate Oxford Instruments SM4-6T and -7T cryogenic superconducting magneto-optical dewars. Samples of ∼1 mM *B. subtilis*, azurin, and amicyanin Cu_A-containing protein fragments were diluted with glycerol-d_3 (∼50% v:v) and injected into sample cells comprised of two quartz disks separated by a Viton O-ring spacer. Similarly, frozen solution (glass) samples of the synthetic dimers were prepared by dissolving the samples anaerobically in rigorously deoxygenated solvent mixtures of either 8:1 MeOH/EtOH or 1:1 propionitrile/butyronitrile, injecting these solutions into Viton O-ring cells, and rapidly freezing the samples. Solid samples (mulls) for absorption and MCD consisted of suspensions of powdered sample in poly(dimethylsiloxane) or Fluorolube mulling agent held between quartz disks. MCD samples were checked for depolarization effects prior to each experiment by monitoring the CD signal of a nickel (+)-tartrate solution placed before and after the sample compartment. All samples used for collection of the data presented displayed negligible (<5%) depolarization effects at liquid helium temperatures. The MCD $\Delta\epsilon$ values reported were obtained by scaling the low-temperature absorption and MCD intensities measured on the same sample to the sample's room-temperature absorption ϵ(max) value.

Vibrational and Resonance Raman Spectroscopy. Resonance Raman spectra were obtained using continuous wave (CW) excitation from Kr^+ (Coherent I90K) and Ar^+ (Coherent I18UV and CR18) ion laser sources. Incident power in the range of ∼5−25 mW was used in a ∼135° backscattering arrangement. Scattering was measured using a SPEX model 1877 CP triple monochromator with 1200, 1800, and 2400 grooves/mm holographic gratings, equipped with a Princeton Instruments back-illuminated CCD detector. Scattering resolution was ∼2 cm^{-1} at all excitation energies. Anaerobic powdered and solution samples were spun in sealed quartz capillary or EPR tubes cooled to ∼120 K using a nitrogen gas flow system. Profile intensities of Raman scattering peaks were determined relative to the 230-cm^{-1} ice peak in protein samples, the 983.6-cm^{-1} scattering peak of K_2SO_4 in solid samples, and the ∼450-cm^{-1} solvent peak in MeOH solution.

Electronic Structure Calculations. The 1982 QCPE package for self-consistent field-Xα-scattered wave (SCF-Xα-SW) calculations[48a] was implemented on IBM 3BT-RS/6000 computers. The atomic exchange parameters, α, were determined by the method of Schwartz.[48b] Inter- and outer-sphere α values were the valence-electron-weighted average of the atomic α values. The atomic sphere radii used here were those previously calibrated to reproduce the experimental *g* values of plastocyanin:[49] Cu, 2.95 b; S(thiolate), 2.50 b; C, 1.80 b; N, 1.90 b; H, 1.17 b (1 bohr (b) ≈ 0.529 Å). In all calculations, N(His or amine) ligands were approximated by NH_3, S(Cys or thiolate) ligands were approximated by SCH_3^-, and the Cu−Cu direction defines the *x*-axis. When included in the calculations, methionine was approximated by dimethyl thioether (H_3CSCH_3) using a S sphere radius of 2.30 b, and the backbone amide oxygen of glutamate was approximated by formaldehyde (H_2CO), with an O sphere radius of 1.37 b and a C radius of 1.60 b. For charged complexes, a Watson sphere was included whose radius was equal to the outer sphere and whose charge was opposite to that of the complex. Complete coordinates and parameters used for all calculations discussed in the text are included in the Supporting Information. Calculations were considered to be converged when the change in potential between subsequent iterations fell below 1×10^{-4} Ry, typically in 400−500 iterations.

An idealized model for the Cu_A active site was constructed using Cu−Cu, Cu−S, and Cu−N radial distances obtained from EXAFS experiments[12,13] and the orientations of N(His) and C^β(Cys) relative to the Cu_2S_2 core approximated from those observed in X-ray crystallographic studies.[14,16] To increase computational throughput, C_i symmetry was imposed. The SCH_3^- protons approximately occupy the positions expected for the two β-methylene protons and C^α in the Cu_A crystal structures. No axial ligands were included in this model. Lifting the C_i symmetry constraint, calculations were also performed using the C_1 crystallographic coordinates of Cu_A from beef heart C*c*O deposited in the Protein Data Bank[50,51] (1OCC), both with (Cu−S(Met) = 2.48 Å; Cu−O(Glu) = 2.19 Å) and without axial ligands. To calculate the electronic structures of the MV and II,II models, the crystallographic coordinates for the Cu, N, and S atoms in these complexes were used. The MV model is rigorously C_i symmetric,[52] while the II,II model has C_2 symmetry.

Results

Cu_A-Type Centers. (A) Electronic Absorption, MCD, and CD Spectroscopies. Figure 1 shows the low-temperature absorption, MCD, and room-temperature CD spectra of the wild-type *B. subtilis*, engineered azurin, and engineered amicyanin Cu_A centers between 4000 and 32 000 cm^{-1}. The 5 K absorption spectra of all three centers are dominated by three intense features at ∼13 400 cm^{-1} (band 3), ∼19 000 (band 6), and ∼21 000 cm^{-1} (band 7), with several additional weaker

(43) Hay, M.; Richards, J.; Lu, Y. *Proc Natl. Acad. Sci. U.S.A.* **1996**, *93*, 461−464.
(44) Dennison, C.; Vijgenboom, E.; de Vries, S.; van der Oost, J.; Canters, G. W. *FEBS Lett.* **1995**, *365*, 92−94.
(45) van der Oost, J.; Lappalainen, P.; Musacchio, A.; Warne, A.; Lemieux, L.; Rumbley, J.; Gennis, J. B.; Aasa, R.; Pascher, T.; Malmström, B. G.; Saraste, M. *EMBO J.* **1992**, *11*, 3209.
(46) Wilmanns, M.; Lappalainen, P.; Kelly, M.; Sauer-Eriksson, E.; Saraste, M. *Proc. Natl. Acad. Sci. U.S.A.* **1995**, *92*, 11955−11959.
(47) Houser, R. P.; Halfen, J. A.; Young, V. G., Jr.; Blackburn, N. J.; Tolman, W. B. *J. Am. Chem. Soc.* **1995**, *117*, 10745−10746.
(48) (a) Cook, M.; Case, D. A. *QCPE* **1991**, *23* 465. (b) Schwartz, K. *Phys. Rev. B* **1972**, *5*, 2466−2468.
(49) Gewirth, A. A.; Solomon, E. I. *J. Am. Chem. Soc.* **1988**, *110*, 3811−3819.
(50) Abola, E. E.; Bernstein, F. C.; Bryant, S. H.; Koetzle, T. F.; Weng, J. In *Crystallographic Databases—Information Content, Software Systems, Scientific Applications*; Allen, F. H., Bergerhoff, G., Sievers, R., Eds.; Data Commission of the International Union of Crystallography: Bonn, 1987; pp 107−132.
(51) Bernstein, F. C.; Koetzle, T. F.; Williams, G. J. B.; E. F. Meyer, J.; Brice, M. D.; Rodgers, J. R.; Kennard, O.; Shimanouchi, T.; Tasumi, M. *J. Mol. Biol.* **1977**, *112*, 535−542.
(52) Average metrical parameters of the two crystallographically distinct MV structures were used.

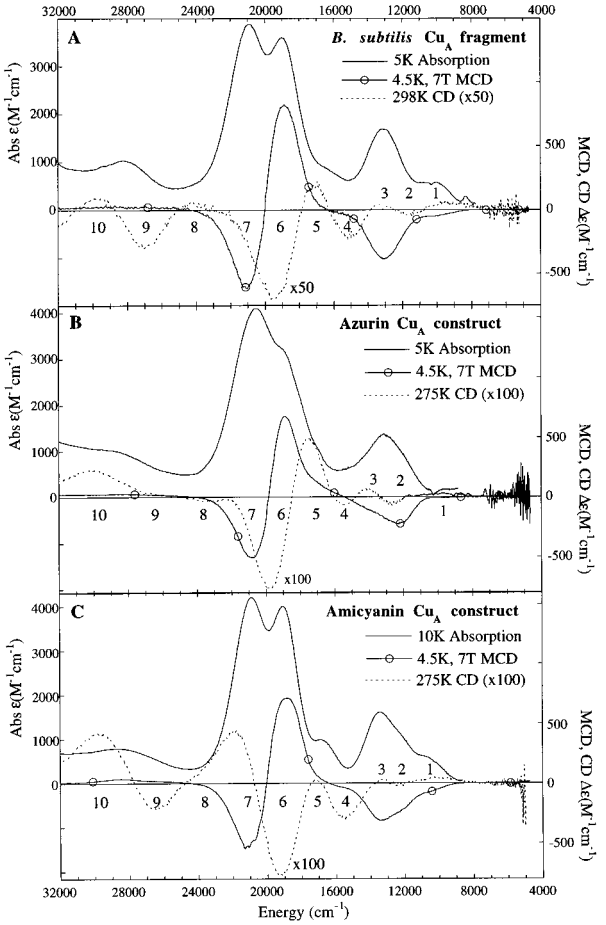

Figure 1. Low-temperature absorption (solid), MCD (solid + circle), and room-temperature CD (dashed) spectra of (A) wild-type Cu_A from *B. subtilis*, (B) azurin Cu_A construct, and (C) amicyanin Cu_A construct.

features also observable both to lower and higher energies. In this range, the MCD and CD spectra reveal at least 10 transitions that are numbered in Figure 1 and parametrized in Table S1 (Supporting Information). The similarities between the spectra in Figure 1 confirm that the engineered azurin and amicyanin Cu_A-type centers are excellent reproductions of the wild-type Cu_A, in contrast with the previously reported purple CyoA,[34] therefore allowing differences to be treated as perturbations over a series of nearly identical structures.

(B) Resonance Raman Spectroscopy. Resonance Raman vibrational spectra obtained for the three Cu_A centers studied were identical to those previously reported for these sites (data not shown).[23] These spectra are all dominated by a ~340-cm^{-1} peak (ν_4), with additional peaks at ~260 (ν_2) and ~270 cm^{-1} (ν_3) and a low-frequency peak at ~130 cm^{-1} (ν_1). Resonance Raman excitation profiles for these Cu_A centers are presented in Figure 2 for the ~340- and ~130-cm^{-1} scattering intensities. The ~260-cm^{-1} peak remains approximately twice as intense as that at ~270 cm^{-1} at every excitation energy, and only their averaged profile intensities are shown in Figure 2 for clarity. For each Cu_A center, the excitation profiles of the ~260-, ~270-, and ~340-cm^{-1} vibrations all behave similarly and roughly follow the absorption spectrum, while the excitation profile of the ~130-cm^{-1} mode differs radically, having its most intense enhancement under band 3 (Figure 2).

Models. (A) Mixed-Valence Model. (i) Absorption and MCD Spectroscopy. Figure 3 presents the low-temperature absorption and MCD spectra of the MV model both in the solid state (Figure 3a) and in a frozen solution (Figure 3b). Five

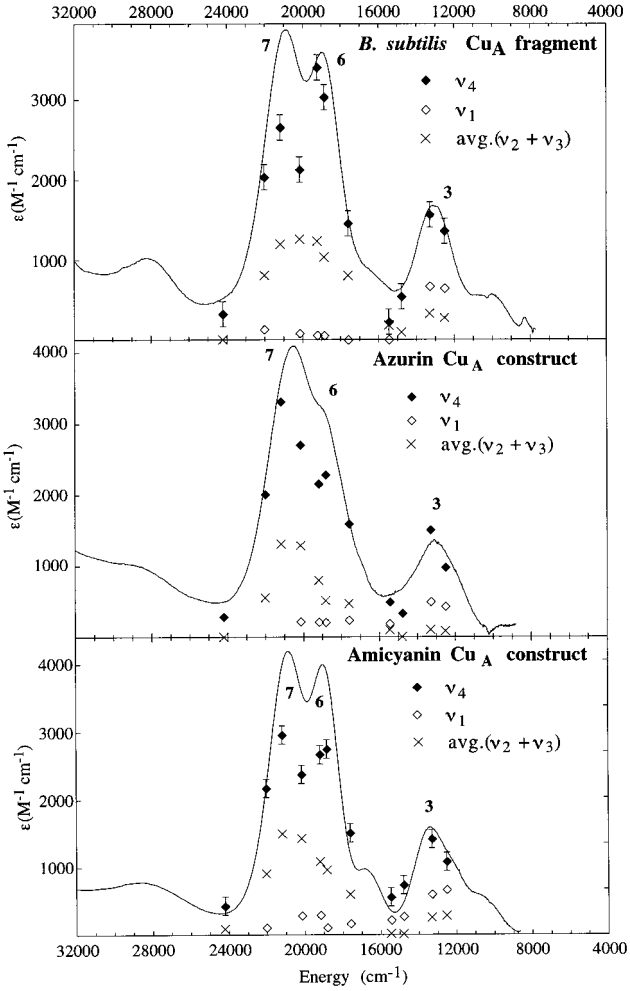

Figure 2. ~120 K resonance Raman excitation profiles of Cu_A sites: (a) wild-type from *B. subtilis*, (b) azurin construct, and (c) amicyanin construct.

absorption and MCD features (bands 1−5) are observed between 4000 and 20 000 cm^{-1} and summarized in Table S2 (Supporting Information). These features all occur ~1400 cm^{-1} higher in energy in frozen solution than in the solid state, indicative of a slight geometric change upon solvation. The near-IR regions of both samples are dominated by an intense absorption feature (band 1) associated with an intense negative MCD feature.

(ii) Resonance Raman Spectroscopy. Figure 4 (inset) shows the resonance Raman vibrational spectrum of the MV model complex obtained with excitation at 647 nm. Similar spectra are obtained using other excitation wavelengths. A series of vibrations is observed between ~130 and 400 cm^{-1}, the most intense of which occurs at ~302 cm^{-1}. Figure 4 shows the intensity of the 302-cm^{-1} peak as a function of excitation wavelength and reveals sizable resonance Raman intensity enhancement with excitation energies greater than ~20 000 cm^{-1}, coinciding with absorption from bands 6 and 7, and relatively little resonance enhancement at energies below ~20 000 cm^{-1} (bands 2−5). Unfortunately, the enhancement behavior resulting from excitation into band 1 was experimentally inaccessible.

(B) Homovalent (II,II) Model. Figure 5 presents the low-temperature solid-state absorption (Figure 5a) and MCD (Figure 5b) spectra of the II,II model. The spectral features observed in this complex are similar to those observed for the MV model (also shown, on the same scale), with the dramatic exception of the intense near-IR feature (band 1). VTVH MCD intensity measurements on this sample reveal an $S = 1$ ground state.[53]

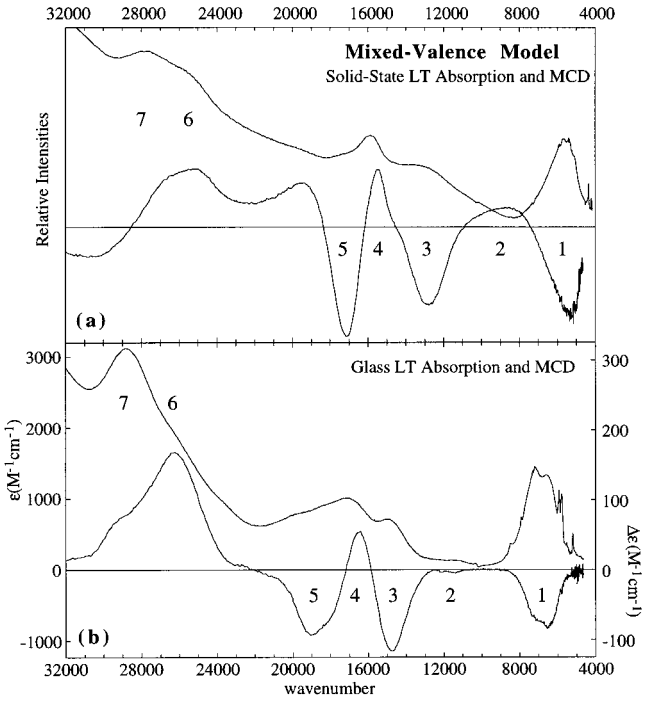

Figure 3. Low-temperature absorption and MCD spectra of the mixed-valence (MV) model: (a) solid mull and (b) frozen solution.

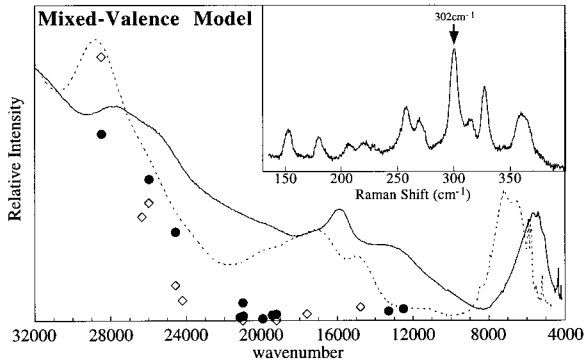

Figure 4. ~120 K solid-state resonance Raman excitation profile of the ~302-cm^{-1} vibration of the mixed-valence (MV) dimer in both solid state (●) and MeOH solution (◇). Inset: ~120 K solid-state Raman vibrational spectrum using 647-nm excitation.

Analysis: $Cu_2(SR)_2$ Molecular Orbital Diagram. As a starting point for this study, a qualitative MO splitting diagram may be constructed by taking symmetric and antisymmetric combinations of the orbitals resulting from a hypothetical monomeric structural fragment $NCu(SR)_2$ (*i.e.*, SALC MOs). The left and right sides of Figure 6 show the d orbital splitting pattern associated with a C_{2v} ML_3 fragment with a basal (unique) angle of ~100°.[54] Combination of these monomeric orbitals forms the dimer MOs shown in the center of Figure 6. As indicated by this figure, the in-plane (Cu_2S_2 plane) *xy* and x^2-y^2 orbitals of the monomeric subunits lie highest in energy due to their strong pseudo-σ antibonding interactions with the in-plane ligand orbitals. These two sets of orbitals are also split most upon dimer formation, which reorients the bridging $S(p_{x,y})$ orbitals and introduces the possibility of direct Cu−Cu bonding interactions. In the current study, the relative energies of the

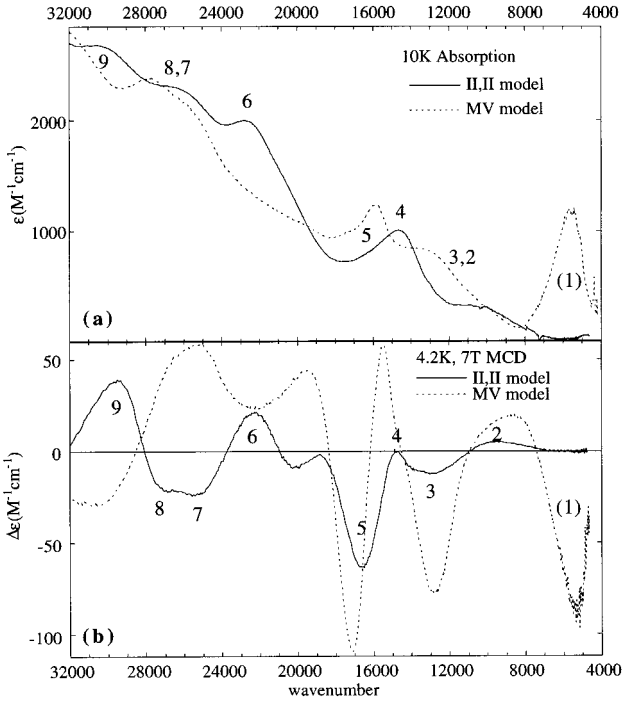

Figure 5. Comparison of the low-temperature solid-state absorption (a) and MCD (b) spectra of the mixed-valence (MV) and homovalent (II,II) model dimers.

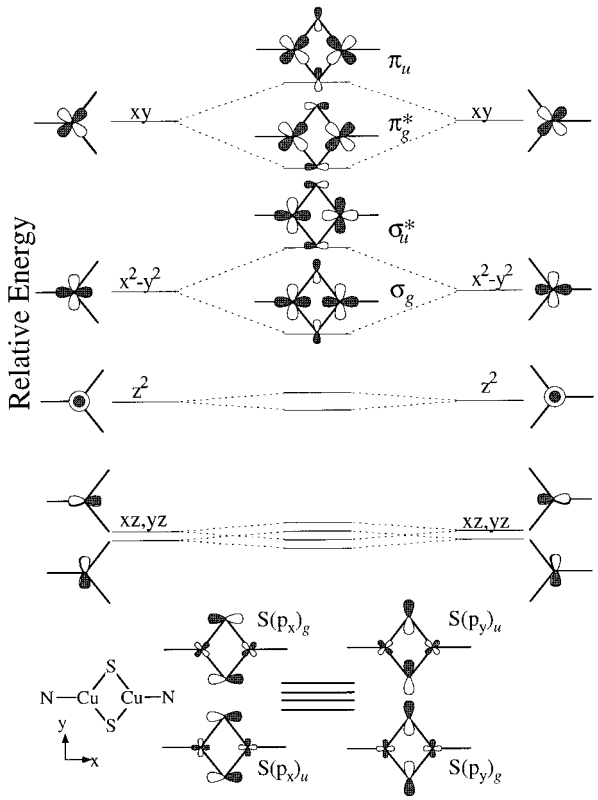

Figure 6. Molecular orbital diagram illustrating the coupling of two C_{2v} CuS_2 fragments (S−Cu−S ≈ 100°) to form a Cu_2S_2 dimer. In the mixed-valence Cu dimers, all MOs are doubly occupied, except for the highest energy orbital shown, which contains only one electron.

MOs in a symmetric and antisymmetric pair depend largely upon the Cu−S−Cu angle, since the thiolate carbons are approximately perpendicular to the Cu_2S_2 plane. At Cu−S−Cu angles smaller than ~90°, as observed for both Cu_A and the MV model (Chart 1), more Cu−S orbital overlap occurs in the antisym-

(53) Gamelin, D. R.; Randall, D. W.; Hay, M. T.; Houser, R. P.; Mulder, T. C.; Canters, G. W.; de Vries, S.; Tolman, W. B.; Lu, Y.; Solomon, E. I., unpublished results.

(54) Albright, T. A.; Burdett, J. K.; Whangbo, M.-H. *Orbital Interactions in Chemistry*; Wiley & Sons: New York, 1985.

metric (*ungerade*) combinations of *xy* and x^2-y^2 orbitals than in their respective symmetric counterparts, splitting the former to higher energy relative to the latter.[55] Placing the 19 d orbital electrons present in a $Cu^{1.5+} - Cu^{1.5+}$ dimer into the MO diagram in Figure 6 would result in a half-occupied ψ*(HOMO) that originates from the antisymmetric combination of the d_{xy} orbitals from each copper. This ψ*(HOMO) is of the appropriate symmetry for a π-type Cu−Cu interaction and is, therefore, referred to as the π_u orbital, regardless of the magnitude (or even absence) of actual Cu−Cu direct overlap. From the MO diagram in Figure 6, it is seen that a series of five parity-allowed ($g \rightarrow u$) d-orbital-based electronic transitions are anticipated in the mixed-valence Cu dimers, each promoting an electron from a doubly occupied orbital to the half-occupied HOMO. Four additional parity-forbidden ($u \rightarrow u$) transitions may also occur with limited intensities. As shall be seen in the following section, the nature of the ψ*(HOMO) is dependent upon (a) the specific ligand-field characteristics of the monomeric Cu subunits comprising the dimer, (b) the Cu−S dimer bonding interactions, and (c) direct Cu−Cu bonding interactions.

Intermediate in energy in Figure 6 are the out-of-plane z^2, *xz*, and *yz* Cu d orbitals. While the z^2 orbital may have some limited in-plane Cu−S bonding interaction, the *xz*, *yz* pair has none. The z^2 orbital, therefore, occurs higher in energy than the *xz*, *yz* pair. All three out-of-plane orbitals have dimer splittings that are small relative to those of the two in-plane orbitals, d_{xy} and $d_{x^2-y^2}$, as shown in Figure 6.

Deeper in energy are the sulfur-based SALC MOs, two arising from each of the three S(p) orbitals, giving three parity-allowed electronic transitions (S → Cu CT). One S(p) orbital from each sulfur is involved in bonding with the thiolate carbon and is, therefore, expected to be significantly deeper in energy, such that transitions from these two S(p) orbitals will not be observed in the spectral region investigated. In both Cu_A and the MV model, the thiolate carbons are approximately perpendicular to the plane of the Cu_2S_2 core (Chart 1), and the two S(p) orbitals available for bonding with the coppers are, therefore, approximately in the *xy* plane. Thus, two parity-allowed and two parity-forbidden $S(p_{x,y}) \rightarrow$ Cu ψ*(HOMO) CT transitions are anticipated. These four in-plane S(p) SALC MOs are depicted in Figure 6, bottom.

Model Complexes. (A) Excited-State Band Assignments. Direct comparison of the low-temperature absorption and MCD spectra for the MV and II,II models (Figure 5) reveals that four of the first five transitions (bands 2−5) are conserved between the two complexes, whereas the intense low-energy feature (band 1) is present only in the MV model. This unambiguously identifies band 1 as the class III mixed-valence $\psi \rightarrow \psi$* transition associated with valence delocalization in this dimer.[56,57] The relatively small resonance Raman intensity enhancement between 12 000 and 22 000 cm^{-1} in the MV model (Figure 4) allows assignment of bands 2−5 as the remaining four parity-allowed d-based electronic transitions. For specific orbital assignments of these transitions in the MV model, its spectral similarity to the II,II model is relied upon. The II,II model consists of two five-coordinate pseudo-square-pyramidal Cu ions separated by 3.34 Å that are tilted with respect to one another by ∼34° (Chart 1C). These factors, along with the observation of an $S = 1$ ground state in this dimer, indicate that the spectroscopy of this system may be analyzed in terms of monomeric MO diagrams, *i.e.*, the dimer splittings shown in the center of Figure 6 are small. On the basis of their pseudo-square-pyramidal ligand field, the hypothetical monomeric halves of this II,II model are expected to have d_{xy} highest in energy, followed by d_{z^2}, and then $d_{x^2-y^2}$, d_{xz}, and d_{yz}. The monomeric ligand-field geometry in this dimer further exhibits a pseudo-D_{2d} distortion, with the $N_{eq}-Cu-N_{eq}$ plane rotated asymmetrically ∼13° relative to that of the S−Cu−S plane. Using D_{2d} selection rules, the MCD signs of the ligand-field transitions to a d_{xy} HOMO can be determined from group theory to be z^2 (+), x^2-y^2 (−), and *xz*,*yz* (±,∓).[49] These allow assignment of bands 2−5 in the II,II model: band 2, z^2; band 3, x^2-y^2; bands 4 and 5, *xz*,*yz*. On the basis of the nearly superimposable II,II and MV model MCD spectra shown in Figure 5, bands 2−5 in the MV model are assigned analogously, implicating a d_{xy}-based ψ*(HOMO) for the MV model as well. Figure 6 shows that a Cu_2S_2 rhomb with Cu−S−Cu angles of 80° (S−Cu−S = 100°) as observed in the MV model is expected to have the π_u MO split higher in energy than the π^*_g MO (*vide supra*), and the MV model is, therefore, concluded to have a π_u orbital ground state.

The two intense absorption features at energies above 22 000 cm^{-1} in the MV model (bands 6 and 7, Figure 3), which are associated with the resonance Raman intensity enhancement shown in Figure 4, are assigned as $S(p_{x,y}) \rightarrow$ Cu ψ*(HOMO) CT transitions. As shown in Figure 6, the π_u(HOMO) in a D_{2h} dimer has contributions from $S(p_y)$ but not $S(p_x)$, while in the real C_i geometry of the MV model this distinction is relaxed somewhat. On the basis of ligand−ligand overlap magnitudes, the more intense, higher energy CT absorption feature (band 7) is assigned as the $S(p_y)_g \rightarrow Cu(\pi_u)$ CT transition, while the weaker absorption shoulder at lower energy (band 6) is assigned as the $S(p_x)_g \rightarrow Cu(\pi_u)$ CT transition, which is parity allowed but has significantly less ligand−ligand overlap contribution to its absorption intensity.

Additional weak features are observed between bands 5 and 6 in the solid-state absorption and MCD spectra of both dimers (Figures 3a and 5). In the MV model, these features appear to diminish in intensity or disappear upon solvation of the sample (Figure 3b) relative to bands 1−7 and are possibly attributable to parity-forbidden transitions of this species.

(B) Xα-SW Molecular Orbital Calculations. Quantitative descriptions of the electronic wavefunctions and orbital splitting patterns are obtained from Xα-SW MO calculations. Table 1 summarizes the calculated MO energies and wavefunction descriptions for the MV model and compares these to the experimentally derived band assignments and energies. Figure 7 shows contours of selected MOs. This MO splitting pattern is similar to that calculated for the II,II model (not shown), with the important exception that the two pairs of dimer orbitals derived from the *xy* and x^2-y^2 parent orbitals are now split significantly by increased dimer interactions resulting from the planarity of the Cu_2S_2 core and compression of the Cu−S−Cu angle from 91.5° to 80°. The calculated ψ*(HOMO) for the MV model has Cu−Cu π_u symmetry and involves significant in-plane sulfur character oriented along the *y* axis ($S(p_y)$) (Figure 7A), consistent with that determined experimentally. The Xα-SW-calculated total S covalency in the π_u(HOMO) of the MV model is 23%, which is in reasonable agreement with the experimental value of 28 ± 3% determined by S K-edge XAS.[35] The deeper, doubly occupied ψ orbital has Cu−Cu π^*_g symmetry and significant $S(p_x)$ character (Figure 7B). The

(55) Hay, P. J.; Thibeault, J. C.; Hoffmann, R. *J. Am. Chem. Soc.* **1975**, *97*, 4884−4899.

(56) Gamelin, D. R.; Bominaar, E. L.; Mathonière, C.; Kirk, M. L.; Wieghardt, K.; Girerd, J.-J.; Solomon, E. I. *Inorg. Chem.* **1996**, *35*, 4323−4335.

(57) Gamelin, D. R.; Bominaar, E. L.; Kirk, M. L.; Wieghardt, K.; Solomon, E. I. *J. Am. Chem. Soc.* **1996**, *118*, 8085−8097.

Table 1. SCF-Xα-SW Description of the Mixed-Valence (MV) Model

				Cu (%)												
		transition energy			*l* breakdown[d]			d m_l breakdown[e]					S (%)		N_{eq}	N_{ax}
orbital label	energy (eV)	calcd[a,b]	exptl[b]	Cu[c]	s	p	d	$d_{x^2-y^2}$	d_{xz}	d_{z^2}	d_{yz}	d_{xy}	S[f]	CH_3[g]	(%)[f]	(%)[f]
π_u	−1.180			69	*0*	*7*	*60*	1.6	3.4	3.4	0.5	51.2	23	1	2	4
π_g*	−1.642	4 870	5 600	75	*1*	*7*	*65*	2.1	15.6	19.5	3.8	23.5	9	0	3	12
σ_u*	−1.185	5 210		77	*1*	*4*	*70*	56.2	0.0	11.1	2.3	0.2	16	1	2	3
$(d_{z^2})_u$	−2.321	9 660		87	*0*	*6*	*81*	0.4	10.3	27.7	0.4	41.9	4	1	2	5
$(d_{z^2})_g$	−2.326	9 730	10 000	83	*0*	*8*	*74*	16.8	7.3	37.7	3.0	9.0	12	1	0	3
$(d_{xz})_g$	−2.680	13 090	15 000	91	*1*	*0*	*90*	14.3	5.7	2.2	65.3	2.0	5	2	1	0
$(d_{yz})_g$	−2.762	13 640	17 000	96	*2*	*0*	*93*	5.6	62.1	22.9	1.9	0.6	3	0	0	0
$(d_{xz})_u$	−2.858	14 500		97	*0*	*0*	*97*	1.6	15.9	1.4	77.5	0.4	1	0	0	0
$(d_{yz})_u$	−2.895	14 620		94	*1*	*0*	*92*	2.5	56.8	20.8	10.3	2.1	3	2	0	1
σ_g	−3.032	15 800	12 800	96	*0*	*0*	*95*	67.4	0.0	7.5	18.0	2.3	3	1	0	0
$S(p_y)_u$	−4.541	28 700		40	*0*	*5*	*32*	0.0	2.9	0.4	0.0	28.9	56	3	1	0
$S(p_x)_g$	−4.624	29 600	26 200	39	*0*	*11*	*27*	1.7	0.5	3.9	2.9	18.1	54	5	0	2
$S(p_y)_g$	−4.872	31 450	28 700	38	*0*	*13*	*24*	2.3	0.9	8.7	0.0	12.2	49	3	1	8
$S(p_x)_u$	−4.968	31 770		47	*2*	*6*	*36*	15.1	1.0	17.1	2.3	0.9	34	2	1	16

[a] Transition energy from transition-state calculation. [b] Calculated and experimental transition energies in cm^{-1}. [c] Total charge on Cu ions. [d] *l* quantum breakdown for Cu. [e] d orbital composition of the Cu d character. [f] Total charge on the S or N atoms; no charge is localized on the ammine protons. [g] Total charge in the CH_3 group.

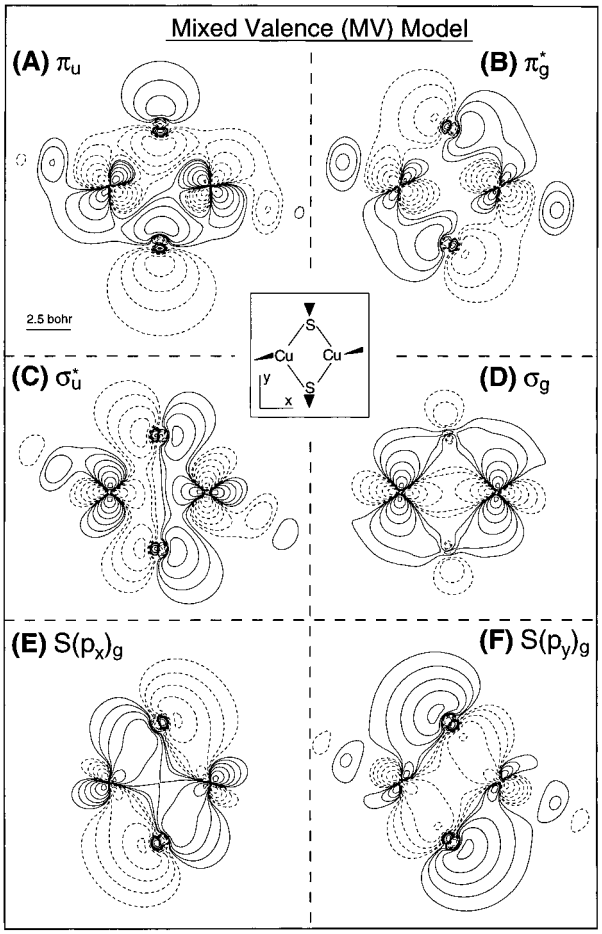

Figure 7. Xα-SW wave function amplitude contour plots of the half-occupied HOMO (π_u) of the mixed-valence (MV) model, its doubly occupied counterpart (π^*_g), the two doubly occupied MOs, σ^*_u and σ_g, and the two $S(p_{x,y})_g$ orbitals. All plots represent contour slices in a plane containing the two Cu atoms as well as the two S atoms, with contour values of ±0.64, ±0.32, ±0.16, ±0.08, ±0.04, ±0.02, and ±0.01 $(e/b^3)^{1/2}$.

calculated energy of the transition between these two orbitals is 4870 cm^{-1}, in agreement with the experimental assignment of a low-energy $\pi^*_g \rightarrow \pi_u$ transition at 5560 cm^{-1} (band 1) in the solid-state geometry. These two orbitals are analogous to the two orbitals calculated to be highest in energy in the II,II model (not shown), consistent with the experimental band assignments for this dimer.[53] The next parity-allowed electronic transition is calculated to derive from the z^2 orbitals and is predicted to occur at ∼9730 cm^{-1}, similar to the ∼10 000 cm^{-1} experimental value. Deeper in energy are the *xz*,*yz* pair, with transitions predicted to occur at ∼13 090 and 13 640 cm^{-1} and observed at ∼15 000 and ∼17 000 cm^{-1}. The transition arising from the symmetric x^2-y^2 combination orbital (σ_g) is predicted to occur at 15 800 cm^{-1} and to be the highest energy Cu-based transition in this dimer. Experimentally, this transition is observed at 12 800 cm^{-1} (band 3), at lower energy than those originating from the *xz*,*yz* pair. The calculated *xy* and x^2-y^2 dimer splittings ($\pi^*_g-\pi_u$ and $\sigma_g-\sigma^*_u$, respectively) are substantially larger than those of the out-of-plane *xz*, *yz*, and z^2 orbitals, as anticipated from Figure 6. This is due to the significantly stronger bonding of the bridging sulfur ligands with these in-plane d orbitals than with the out-of-plane orbitals. Xα-SW predicts the $\pi^*_g-\pi_u$ splitting to be 4870 cm^{-1} and the $\sigma_g-\sigma^*_u$ splitting to be 10 600 cm^{-1}. While the calculated $\pi^*_g-\pi_u$ splitting is confirmed by experiment (4870 *vs* 5560 cm^{-1}), no experimental estimate of the $\sigma_g-\sigma^*_u$ splitting magnitude is available, except to note that the experimental band assignments indicate that the *xz*, *yz* pair is deeper than the σ_g orbital, and the $\sigma-\sigma^*$ splitting is, therefore, likely smaller than the calculated value. The calculated *xz*, *yz*, and z^2 splittings in the MV model are each less than ∼1500 cm^{-1}.

Deeper in energy, the two $S(p_{x,y})_g \rightarrow$ Cu π_u(HOMO) CT transitions are predicted to occur at 29 600 $(S(p_x)_g)$ and 31 400 cm^{-1} $(S(p_y)_g)$, compared with the experimental values of 26 200 and 28 700 cm^{-1}, respectively. In contrast with the S-based orbitals shown in Figure 6, however, the Xα-SW contours for these two S-based MOs (Figure 7E,F) show the effect of symmetry reduction and are no longer pure $S(p_x)$ or $S(p_y)$ in character. This may account for the ∼3:1 absorption intensity ratio of bands 7:6 (*vide infra*).

Cu_A Sites. (A) Excited-State Band Assignments. As can be seen in Figure 1, absorption, MCD, and CD spectroscopies identify a series of 10 electronic transitions of the Cu_A site in the range from 4000 to 32 000 cm^{-1}. Bands 6 and 7 are assigned as $S(p_{x,y}) \rightarrow$ Cu(HOMO) CT transitions on the basis of their absorption intensities and resonance Raman excitation profiles (Figure 2), which show strong enhancement of Cu−S stretching vibrations. The five electronic transitions (bands 1−5) observed to lower energy of these CT transitions are

Chart 2

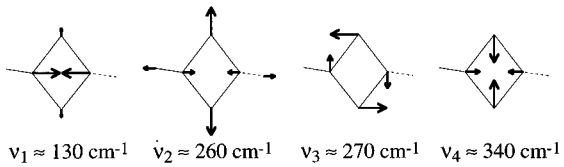

associated with the five parity-allowed d-orbital-based transitions expected on the basis of the MO model shown in Figure 6, and we address their specific assignments first.

Near-IR resonance Raman measurements show a dramatically different intensity distribution from that obtained with excitation into bands 6 and 7.[58] Specifically, Figure 2 shows that excitation into bands 6 and 7 leads to strong resonance enhancement of the Cu_2S_2 core breathing mode at ~340 cm^{-1} (ν_4), a mixed Cu−S/Cu−N stretching mode at ~260 cm^{-1} (ν_2), and an out-of-phase "twisting" Cu−S stretching mode at ~270 cm^{-1} (ν_3), described previously[17] and illustrated in Chart 2. Excitation into band 3 also strongly enhances Cu_A vibrations, but Figure 2 shows that this enhancement involves a decrease of the ν_2 and ν_3 intensities and a significant increase in the ~130-cm^{-1} intensity (ν_1), relative to the intensity of ν_4. This ~130-cm^{-1} vibration has been assigned as the Cu_2S_2 core "accordion" bending mode (Chart 2),[17,58] involving motion of the two copper nuclei, and its strong resonance enhancement with excitation into band 3 indicates that the Cu_A site undergoes a significant change in Cu−Cu separation in this excited state. This observation is the basis for assignment of band 3 as the mixed-valence $\psi \rightarrow \psi^*$ transition associated with Cu_A valence delocalization.[35,58] Comparison of these data to those of another delocalized class III dimer, $[Fe_2(OH)_3(tmtacn)_2]^{2+}$, shows that both the significant absorption intensity and specific resonance Raman behavior of band 3 in Cu_A are consistent with those anticipated for the $\psi \rightarrow \psi^*$ transition of this site.[56,57]

Figure 8 compares the low-temperature absorption and MCD spectra of the *B. subtilis* Cu_A site with those of the MV model in frozen solution. One of the salient differences between the MV model and Cu_A spectra shown in Figure 8a is the dramatic increase in the $\psi \rightarrow \psi^*$ transition energy from ~5560 cm^{-1} in the MV model (solid state, or 6760 cm^{-1} in solution as shown in Figure 8) to ~13 400 cm^{-1} in Cu_A. Since the ~2.92-Å Cu−Cu separation in the MV model is too large for significant direct π-type Cu−Cu overlap to occur, the $\psi \rightarrow \psi^*$ splitting observed in this dimer must result from Cu−S interactions only. Sulfur K-edge X-ray absorption experiments on *B. subtilis* Cu_A and the MV model show that the %S covalencies in the ψ^*(HOMO) orbitals of the MV model (in the solid state) and *B. subtilis* Cu_A are the same (26 ± 3% in Cu_A *vs* 28 ± 3% in the MV model),[35] ruling out the possibility that the large difference in $\psi \rightarrow \psi^*$ energies is due to a large change in Cu−S contributions between these structures. The difference in $\psi \rightarrow \psi^*$ splitting energies is, therefore, attributed to the presence of direct Cu−Cu overlap in Cu_A, made possible by the short, ~2.44-Å Cu−Cu separation. Using the 5560-cm^{-1} splitting observed in the MV model (solid state) as an estimate of the Cu−S contribution to the $\psi \rightarrow \psi^*$ splitting in Cu_A, this direct Cu−Cu bonding interaction is estimated to contribute approximately 7800 cm^{-1}, or ~59%, to the total splitting energy. Inspection of the two in-plane dimer SALC orbitals in Figure 6 shows that introduction of a direct Cu−Cu bonding interaction destabilizes the σ^*_u MO and stabilizes the σ_g MO, thus increasing the $\sigma_g - \sigma^*_u$ pair splitting, whereas direct Cu−Cu bonding should decrease the $\pi^*_g - \pi_u$ pair splitting. Recalling the increase in $\psi \rightarrow \psi^*$ transition energy in Cu_A relative to the MV model, this analysis leads to the conclusion that the ψ^*(HOMO) of Cu_A has significant σ^*_u character, in contrast to the MV model with a π_u HOMO. This analysis also indicates that valence delocalization in Cu_A involves substantial direct Cu−Cu σ-bonding between the $d_{x^2-y^2}$ orbitals of the two Cu ions. Note that the reduction in symmetry from that in Figure 6 (D_{2h}) to that in the Cu_A protein environment (~C_i) relaxes the rigorous σ/π MO descriptions shown in Figure 6, allowing some mixing of orbitals having the same parity (*vide infra*).

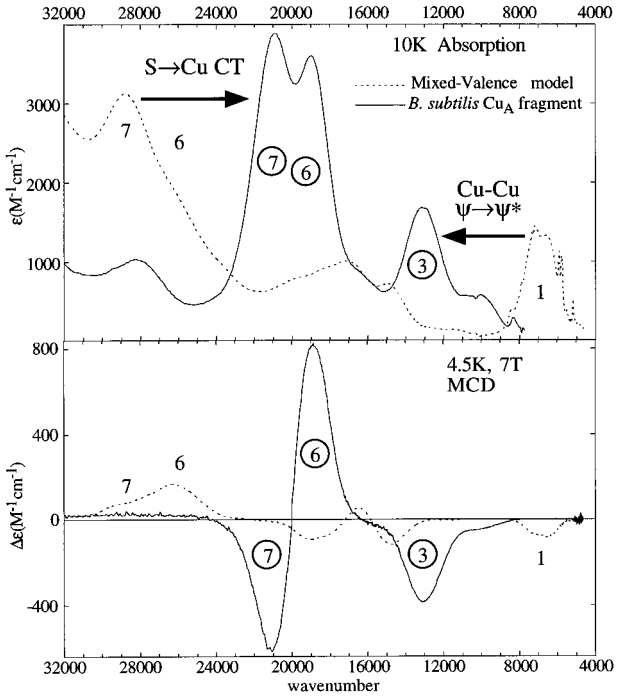

Figure 8. Comparison of low-temperature absorption (a) and MCD (b) spectra of the mixed-valence model (frozen solution) and wild-type Cu_A from *B. subtilis*.

We now address the remaining four d-based transitions of Cu_A. Of the two transitions observed lower in energy than band 3 in Figure 1, band 1 is more intense and is, therefore, associated with the in-plane π^*_g MO, which would involve more S($p_{x,y}$) mixing: band 1 is assigned as the $\pi^*_g \rightarrow \sigma^*_u$(HOMO) transition. Band 2, which is observed in all three Cu_A sites studied here and has not been previously reported, is then assigned as the $(z^2 + z^2)_g \rightarrow \sigma^*_u$(HOMO) transition. Bands 4 and 5, higher in energy than band 3, are assigned as transitions from the *xz*,*yz* pair SALC MOs on the basis of their deeper energy, their similar bandshapes, and their opposite signs in the MCD and CD spectroscopies. Band 5 has more absorption intensity than Band 4 and is, therefore, assigned as the $(yz + yz)_g \rightarrow \sigma^*_u$(HOMO) transition, since in D_{2h} symmetry only the $(yz + yz)_g$ SALC MO is of appropriate symmetry to mix with any S(p) orbitals (S(p_z)), and in lower symmetry this mixing still dominates due to the ~116° S−Cu−S angle, which places the S ligands significantly closer to the *y* axis than to the *x* axis.

A second striking difference is observed in Figure 8 between the spectra of the MV model and those of the Cu_A site, namely the reduction in energy from ~28 000 to ~20 000 cm^{-1} of the intense S($p_{x,y}$) → Cu CT absorption features. This shift parallels that observed in blue copper proteins relative to monothiolate model complexes and is directly related to the weakened axial bonding interaction in Cu_A; the loss of a donor ligand stabilizes

(58) Wallace-Williams, S. E.; James, C. A.; de Vries, S.; Saraste, M.; Lappalainen, P.; van der Oost, J.; Fabian, M.; Palmer, G.; Woodruff, W. H. *J. Am. Chem. Soc.* **1996**, *118*, 3986−3987.

Table 2. Comparison of Correlated Physical Properties for Plastocyanin, Cu_A, and Their Models

	coordination number	CT energy (cm^{-1})	S K-edge preedge energy (eV)	reduction potential (mV vs NHE)
Pc^{2+}	~3 (+1 weak)	~17 500[a]	2469.0[b]	+370[c]
Cu(tet*b*)$^{2+}$	5	~28 000[d]	2470.0[b]	na
Cu_A^+	~3 (+1 weak)	~20 000	2469.8[e]	+240[f]
MV model	4	~28 000	2470.0[e]	−280[g]

[a] Reference 49. [b] Reference 60. [c] Reference 61. [d] Reference 59. [e] Reference 35. [f] References 2, 39, 62, and 63. [g] Reference 42.

the Cu d orbitals relative to the S(p) orbitals, thereby reducing the S(p) → Cu d CT energies. Table 2 summarizes the correlation between coordination number, CT energies, and other physical properties for oxidized plastocyanin, mixed-valence Cu_A, and their models. For both the monomeric and dimeric systems, Table 2 demonstrates that removal of a ligand stabilizes the Cu d orbitals, which in turn shifts the CT transitions down in energy, as observed in both UV/vis absorption[49,59] and S K-edge XAS[35,60] experiments, and drives the reduction potential more positive.[2,39,61−63] Thus, the distinctive purple color of the Cu_A site has the same fundamental origin as the blue color of blue copper centers, namely highly covalent Cu−S(Cys) bonding interactions that lead to intense CT transitions, and reduction in energy of these CT transitions relative to model complexes due to a diminished Cu coordination number of <4 in both systems.

Three transitions (bands 8−10 in Figure 1) are observed higher in energy than the dominant CT transitions (bands 6 and 7). Bands 8 and 10 have previously been assigned as parity-forbidden S → Cu CT transitions, while band 9 has been assigned as the parity-allowed $(z^2 + z^2)_g \rightarrow \psi^*$(HOMO) transition.[34] Resonance Raman experiments show no ν_4 enhancement with excitation into band 10.[24] Preliminary resonance Raman data do, however, show intensity in a histidine ring mode at ~1410 cm^{-1} with 28 000-cm^{-1} excitation,[53] but all three Cu_A sites studied here are too susceptible to photodecomposition in this region for excitation profiling. This ~1410-cm^{-1} Raman intensity is believed to be associated with the Cu_A, since its intensity diminishes with bleaching of the sample's purple color. On the basis of these observations, the assignment of bands 9 and 10 as N(His) → Cu CT transitions is preferred. These two transitions from the two inequivalent histidine ligands should occur at similar energies but are expected to have different absorption intensities due to their differing covalencies (observed by ENDOR[28]). CNDO calculations on the bovine heart C*c*O Cu_A structure including the full histidine rings suggest that the histidine bound to the same Cu as the axial methionine, *i.e.*, H161,[64] is the more covalent of the two terminal histidines,[33] and paramagnetic NMR studies of the amicyanin Cu_A construct also show approximately 2 times the electron density on the histidine *cis* to the methionine as on that *cis* to the glutamate amide.[30] Since the majority of the absorption intensity in this region derives from band 10 (Figure 1, Table S1), this transition is associated with the more covalent N(His) ligand of the Cu_A site and is, therefore, assigned as a H161 → Cu CT transition.[64] Band 9 is weaker in absorption and is assigned as the H204 → Cu CT transition.[64] Since H204 is proximal to heme *a*, its smaller covalency has significant implications in relation to the Cu_A → heme *a* ET pathway, which has been proposed[14,15,65] to proceed via this histidine (see Discussion). These His → Cu CT transitions are reduced in energy relative to those found in synthetic Cu-His-type model complexes[66] for the same reason as are the S → Cu CT bands, namely due to the reduced coordination number of the Cu ions in the Cu_A site. Band 8 is difficult to assign as it has little absorption, MCD, or CD intensity, but it may be a parity-forbidden CT transition or a weak CT transition originating from the axial methionine.

(B) Xα-SW Molecular Orbital Calculations. The results from Xα-SW MO calculations on a C_i-idealized Cu_A structure are summarized in Table 3, which also includes a comparison between calculated and experimental transition energies. These calculations predict a ψ^*(HOMO) for Cu_A having significant σ^*_u character, in agreement with experiment, and a $\sigma_g \rightarrow \sigma^*_u$-(HOMO) transition-state energy of 17 060 cm^{-1}, larger than, but still in reasonable agreement with, the value obtained experimentally of ~13 400 cm^{-1}. The contours for these two MOs are shown in Figure 9A,D, along with the contours for the π_u and π^*_g orbitals (Figure 9B,C) and the two $S(p_{x,y})_g$ MOs (Figure 9E,F). The calculation predicts 25% total S character and 4% total N character in the HOMO, in excellent agreement with the values of 26 ± 3% S[35] and ~4% N[28] determined experimentally. The calculation predicts that the $\sigma_g \rightarrow \sigma^*_u$ transition (band 3) should be the highest energy d-based electronic transition, in contrast with the experimental observation of two d-based transitions at higher energy (bands 4 and 5). Consistent with the behavior anticipated from the MO diagram in Figure 6, the dimer splittings of the in-plane orbitals ($\sigma_g-\sigma^*_u$ (17 100 cm^{-1}) and $\pi^*_g-\pi_u$ (6400 cm^{-1})) are calculated to be greater than those of the out-of-plane combination orbitals, although the *xz* pair splitting (~6160 cm^{-1}) is also large. The large calculated splitting of the *xz* pair, as well as the large $\sigma_g-\sigma^*_u$ splitting, likely reflects a small overestimation of direct Cu−Cu bonding interactions in this calculation. The small splitting calculated for the z^2 pair (~900 cm^{-1}) is inconsistent with previous INDO/S calculations,[34] which suggest that the splitting between the symmetric and antisymmetric z^2 combination orbitals is >10 000 cm^{-1} and lead to assignment of band 8 as the parity-allowed transition from this pair. The observation of five low-energy transitions yields a ligand-field molecular orbital diagram that is consistent with that anticipated for the crystallographic coordination geometry (*vide infra*) and avoids the necessity to assign band 8 as a d-based transition.

To explore the effects of lifting the artificial C_i symmetry imposed on the Cu_A center, Xα-SW calculations were also performed using the bovine heart C*c*O Cu_A crystallographic coordinates without axial ligands.[15,16] A table (S3) containing the results of this calculation and select orbital contours are included in the Supporting Information. The calculated HOMO is similar to that shown in Figure 9A and is predominately $d_{x^2-y^2}$ (>85% of the Cu d character), giving a σ^*_u-like ground state, as was the case for the idealized structure discussed above. An interesting aspect of this C_1 calculation relates to the slight asymmetric charge distribution within the Cu_A core: 32% of the total HOMO spin density is on the Cu adjacent to H161,

(59) Hughey, J. L. I.; Fawcett, T. G.; Rudich, S. M.; Lalancette, R. A.; Potenza, J. A.; Schugar, H. J. *J. Am. Chem. Soc.* **1979**, *101*, 2617−2623.
(60) Shadle, S. E.; Penner-Hahn, J. E.; Schugar, H. J.; Hedman, B.; Hodgson, K. O.; Solomon, E. I. *J. Am. Chem. Soc.* **1993**, *115*, 767−776.
(61) Solomon, E. I.; Baldwin, M. J.; Lowery, M. D. *Chem. Rev.* **1992**, *92*, 521−542.
(62) Reister, J.; Kroneck, P. M. H.; Zumft, W. G. *Eur. J. Biochem.* **1989**, *178*, 751−762.
(63) Morgan, J. E.; Wilkström, M. *Biochemistry* **1991**, *30*, 948−958.
(64) Sequence numbering scheme from bovine heart C*c*O (refs 15 and 16, PDB 1OCC).
(65) Ramirez, B. E.; Malmström, B. G.; Winkler, J. R.; Gray, H. B. *Proc. Natl. Acad. Sci. U.S.A.* **1995**, *92*, 11949−11951.
(66) Schugar, H. J. In *Copper Coordination Chemistry: Biochemical and Inorganic Perspectives*; Karlin, K. D., Zubieta, J., Eds.; Adenine Press: New York, 1982; pp 43−74.

Table 3. SCF-Xα-SW Description of C_i-Idealized Cu_A

				Cu (%)									S (%)		
	energy	transition energy			*l* breakdown[d]			d m_l breakdown[e]							
orbital label	(eV)	calcd[a,b]	exptl[b]	Cu[c]	s	p	d	$d_{x^2-y^2}$	d_{xz}	d_{z^2}	d_{yz}	d_{xy}	S[f]	Cys[g]	N (%)[f]
σ_u*	−1.751			70	*0*	*1*	*67*	57.3	4.4	0.5	0.2	4.1	25	2	4
π_u	−2.148	3 230	(∼3 500)[h]	72	*1*	*11*	*59*	5.4	0.1	0.1	0.1	53.4	25	2	1
$(d_{xz})_g$	−2.788	8 850	16 000	94	*0*	*6*	*87*	5.0	68.1	2.2	0.0	12.1	2	0	3
π_g*	−2.925	9 630	9 500	84	*0*	*6*	*78*	0.4	13.3	0.1	7.6	56.7	13	1	1
$(d_{z^2})_u$	−3.195	12 450		98	*3*	*0*	*94*	3.8	0.1	89.9	0.2	0.0	1	0	1
$(d_{yz})_g$	−3.256	12 420	17 000	87	*3*	*0*	*84*	3.2	1.6	10.8	60.2	8.6	10	3	0
$(d_{z^2})_g$	−3.325	13 360	12 000	97	*6*	*1*	*90*	2.2	5.3	71.8	10.3	0.6	1	1	0
$(d_{yz})_u$	−3.354	13 820		98	*0*	*0*	*98*	0.9	3.2	0.4	93.5	0.1	1	0	0
$(d_{xz})_u$	−3.541	15 010		94	*0*	*1*	*91*	5.2	78.9	0.3	4.6	2.2	3	2	1
σ_g	−3.797	17 060	13 400	94	*0*	*2*	*91*	77.3	4.1	0.6	7.6	1.6	4	0	1
$S(p_x)_g$	−4.371	23 540	21 060	39	*0*	*12*	*25*	0.0	0.0	0.0	5.9	19.0	58	2	0
$S(p_y)_u$	−5.101	28 730		41	*3*	*3*	*33*	5.9	5.1	1.8	0.0	20.0	52	6	0
$S(p_y)_g$	−5.365	31 730	18 800	35	*7*	*11*	*16*	3.2	0.6	7.1	5.4	0.1	55	8	1
$S(p_x)_u$	−5.430	31 100		49	*8*	*2*	*38*	23.2	0.0	4.8	0.0	9.7	47	4	0

[a] Transition energy from transition-state calculation. [b] Calculated and experimental transition energies in cm^{-1}. [c] Total charge on Cu ions. [d] *l* quantum breakdown for Cu. [e] d orbital composition of the Cu d character. [f] Total charge on the S or N atoms; no charge is localized on the ammine protons. [g] Total charge in the CH_3 group. [h] Estimated from quantitative EPR simulations.[37]

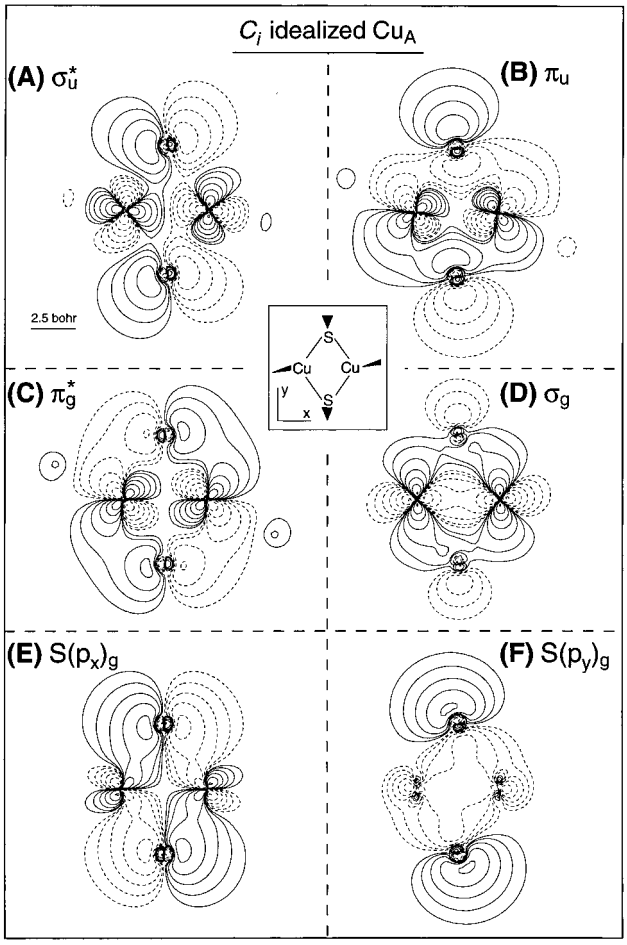

Figure 9. Xα-SW wave function amplitude contour plots for a C_i-idealized Cu_A geometry based on EXAFS and X-ray crystallographic structural parameters. Included are contours of the half-occupied HOMO (σ^*_u), its doubly occupied counterpart (σ_g), two additional doubly occupied MOs, π_u and π^*_g, and the two $S(p_{xy})_g$ orbitals. All plots represent contour slices in a plane containing the two Cu atoms and two S atoms, with contour values of ±0.64, ±0.32, ±0.16, ±0.08, ±0.04, ±0.02, and ±0.01 $(e/b^3)^{1/2}$.

while 39% is on the Cu adjacent to H204.[64] In contrast, the covalency of the sulfurs is more similar, with ∼12% on one and ∼13% on the other, again in excellent agreement with the experimental value of 26 ± 3% total S character.[35] The ligating ammines in the calculation, which abbreviate H161 and H204 ligands in the Cu_A site, also show asymmetric spin density, with ∼1.1% of the total HOMO spin density on N(H161) and ∼1.9% on N(H204). From this low-symmetry calculation, it can be seen that the valence delocalization imposed by the C_i symmetry of the above calculation is also predicted by Xα-SW when not required by the artificial symmetry. Adding the axial ligands at the crystallographic distances (Cu−S(Met) ≈ 2.5 Å; Cu−O(Glu) ≈ 2.2 Å) does not qualitatively alter the HOMO description.

(C) Cu_A Ground State and Its Effect on Spectroscopic Features. The Xα-SW contour of the Cu_A σ^*_u(HOMO) (Figure 9A) shows a key perturbation relative to the analogous σ^*_u orbital of the MV model (Figure 7c), namely the partial rotation of the x^2-y^2 orbital lobes away from the *x* and *y* axes. This effect is attributed to mixing between the σ^*_u and π_u orbitals, allowed in C_i symmetry since they both have the same (*ungerade*) symmetry. The magnitude of such mixing is inversely related to the magnitude of energetic separation between these two orbitals. From Table 3, Xα-SW calculations predict the σ^*_u(HOMO) in Cu_A to be separated by only 3230 cm^{-1} from the next deeper (doubly occupied) orbital, in good agreement with experimental estimates.[32] Concomitant with this is the equal magnitude rotation of the π_u orbitals, as seen in Figure 9B. The absence of significant rotation in the S-based orbitals, as well as in the σ_g and π^*_g orbitals, excludes the possibility[33] that this rotation arises from the specific orientation of the cysteine carbon atom but, instead, supports the assertion that it results from orbital mixing due to the energetic proximity of the σ^*_u and π_u orbitals. Since this rotation alters the character of the redox-active orbital in Cu_A, we are interested in further characterizing it experimentally by evaluating its effects on the spectroscopic properties of this site, in particular the S → Cu CT features of Figure 1.

The presence of this mixed ground state is manifested experimentally by the observation of two intense S(Cys) → Cu CT transitions in the Cu_A absorption spectrum. The absorption intensity of a ligand-to-metal CT transition is related to the magnitude of ionic D^+A^- (as opposed to neutral DA) character present in the ψ*(HOMO) wavefunction.[67] The magnitude of ligand character in the HOMO serves as a measure of this ionic CT character, and an increase in ground-state covalency is

(67) Mulliken, R. S.; Person, W. B. *Molecular Complexes*; Wiley-Interscience: New York, 1969.

generally assumed to lead to greater CT intensities. Of the four in-plane S($p_{x,y}$)-based donor orbital combinations shown in Figure 6, only the two *gerade* combinations will lead to parity-allowed electronic transitions to the *ungerade* σ^*_u HOMO, but only one of these, S(p_x), has any ligand−ligand overlap with the pure σ^*_u orbital of Figure 6. Introduction of mixing between the σ^*_u and π_u MOs results in a HOMO that now has nonzero ligand−ligand overlap with both S(p_x) and S(p_y), such that both parity-allowed S → Cu CT transitions exhibit significant absorption intensity associated with ligand−ligand overlap.[68] Resonance Raman experiments provide an independent experimental indication that this mixing occurs in the Cu_A site: enhancement by both bands 6 and 7 of the Cu_2S_2 twisting vibration (ν_3, Chart 2), which is totally symmetric in C_i (and, therefore, Raman-allowed) but not in D_{2h}, indicates a bonding scheme in which the two Cu−S bonds of each thiolate are distinct but related to those of the other thiolate through inversion symmetry, as occurs upon mixing between the σ^*_u and π_u orbitals in the HOMO. The stronger absorption intensity of band 7 over band 6 in all Cu_A sites studied (Figure 1, Table S1) is the primary basis for assignment of band 7 as the $S(p_x)_g$ → Cu ψ^*(HOMO) CT transition, since the projection of S(p_x) onto the σ^*_u-like HOMO will be larger than that of S(p_y). Band 6 is then assigned as the $S(p_y)_g$ → Cu ψ^*(HOMO) CT transition. Thus, the relative S → Cu CT absorption intensities of Cu_A probe the relative magnitudes of σ^*_u and π_u MO character in the Cu_A ψ^*(HOMO).[69]

This analysis is also consistent with the observation of significantly more CD intensity in band 6 than in band 7. CD intensity requires simultaneously allowed electric and magnetic dipole transition moments. The magnetic dipole transition moments transform with the rotational operators R_x, R_y, and R_z, and the S(Cys) → Cu CT CD intensity is, therefore, expected to be greater for the weaker absorption feature, since this involves more S(p_y) → S(p_x) character (related by R_z) than the stronger absorption feature, which involves more S(p_x) → S(p_x) character. Note that the CD intensity of band 7 is greatest in the amicyanin Cu_A fragment, where the relative CT absorption intensities are closest (∼1.5:1). This correlation presumably occurs because bands 6 and 7 now both involve significant S(p_x) → S(p_y) or S(p_y) → S(p_x) character.[70]

Finally, it is apparent from the comparison of this series of Cu_A sites that the CT absorption and MCD intensities behave differently. Although the relative integrated band 7:band 6 absorption intensities across this series span a range of ∼2.9:1 in azurin Cu_A to ∼1.5:1 in amicyanin Cu_A, the relative integrated MCD intensities of these two transitions remain fairly constant at ∼−0.8: +1. This behavior can be rationalized by recognizing that the electronic properties of the Cu_A HOMO contribute differently to the intensities of the CT bands in the absorption and MCD spectra due to the different selection rules for the two techniques. Specifically, since ligand−ligand overlap contributes most to the absorption intensity, mixing the σ^*_u HOMO with the π_u MO results in a decrease of intense *y*-polarized $S(p_x)_g$ → σ^*_u CT character and a gain of weak *x*-polarized $S(p_x)_g$ → π_u CT absorption character in band 7. Similarly, upon HOMO mixing, band 6 gains intense *y*-polarized $S(p_y)_g$ → π_u CT absorption character at the expense of weak *x*-polarized $S(p_y)_g$ → σ^*_u CT character, and the absorption intensity increases as the mixing increases. This analysis would, therefore, predict that the majority of the absorption intensity observed in both of the intense S(Cys) → Cu ψ^*(HOMO) CT transitions (bands 6 and 7) is polarized along the S−S (*y*) axis.

MCD *C*-term intensity, however, requires the presence of two perpendicular nonzero components of the electric dipole transition moment (M_i) that are additionally both perpendicular to the Zeeman direction[71] (*i.e.*, $\Delta\epsilon \propto g_z M_x M_y + g_x M_y M_z + g_y M_x M_z$). Since all electronic states are nondegenerate in low-symmetry protein sites such as the Cu_A centers studied here, for any given Cu_A electronic transition, at most one M_i component may be nonzero. The observation of *C*-term MCD intensity, therefore, implicates out-of-state spin-orbit coupling (SOC); such coupling allows additional M_i components to become nonzero through mixing of the nondegenerate states.[72] MCD *C*-term intensity dominated by out-of-state SOC between two excited states manifests itself as a pseudo-*A*-term MCD feature, in which the MCD bands associated with the two interacting excited states have equal magnitudes but opposite signs.[72,73] This is clearly the case for bands 6 and 7 of Cu_A (Figure 1). As discussed above, the majority of the absorption intensity in both bands is *y*-polarized, and SOC between this character in the two excited states will not generate the MCD *C*-term intensity since they are collinear rather than perpendicular. Thus, the large *C*-term MCD intensities of bands 6 and 7 in Cu_A must derive from efficient out-of-state SOC of a dominant *y*-polarized component with a smaller *x*-polarized (*i.e.*, Cu−Cu) component, with such efficiency due to their energetic proximity.[34]

Out-of-state SOC of an excited state with the ground state may also give rise to large MCD *C*-term intensities, but, in contrast with intensity derived exclusively from SOC between excited states, this intensity no longer obeys the sum rule.[73] This provides an explanation for a third major difference between the Cu_A and MV model spectra shown in Figure 8, namely the large MCD *C*-term intensities in Cu_A relative to those observed in the MV model: after accounting for the equal and opposite pseudo-*A*-term intensities of bands 6 and 7, the remaining Cu_A-integrated MCD intensity in Figure 8 is predominantly negative, with a ratio of −2.0:1.0, whereas in the MV model the ratio of integrated MCD intensities is −0.8:1.0. Previous studies have shown that the excited state lying ∼3500 cm^{-1} above the HOMO in Cu_A may mix *via* SOC with the HOMO,[34] while the lowest-energy electronic excited state of appropriate parity for spin−orbit coupling with the ground state in the MV model is the σ^*_u state, calculated to occur ∼5200 cm^{-1} above the ground state (Table 1). Thus, the closer energetic proximity of the first excited state in Cu_A relative to the MV model imparts the former with more efficient SOC mixing with the ground state and leads to the larger MCD *C*-term intensities observed in Cu_A.

In summary, the observation of two intense S → Cu CT transitions is one of the principal properties that has long distinguished Cu_A spectroscopy from the spectroscopy of classic blue copper proteins such as plastocyanin, where one $S(p_{x,y})$ → Cu(HOMO) CT transition is dominant and the second is very weak due to vastly differing degrees of ligand−ligand overlap.[49] In the purple Cu_A sites, the total S → Cu CT integrated intensity

(68) Metal−metal overlap is not considered to contribute the majority of intensity to these bands. The metal−metal contribution to the CT intensity is estimated to be less than half of the intensity of band 3 in Figure 1.

(69) The increased band 7:6 absorption ratio of azurin Cu_A (∼2.9:1) suggests that this ψ^*(HOMO) is more purely σ^*_u than those of the wild-type or amicyanin Cu_A sites (bands 7:6 ≈ 1.5−1.7:1). This must result from an increase in the energetic separation between the σ^*_u and π_u orbitals and could have its origin in the reported contraction of the Cu−Cu separation by ∼0.05 Å relative to the *B. subtilis* Cu_A,[74] although other structural changes may also contribute (vide infra).

(70) An empirical correlation between EPR hyperfine structure and relative absorption intensities of bands 6 and 7 has been previously noted.[43]

(71) Piepho, S. B.; Schatz, P. N. *Group Theory in Spectroscopy*; Wiley-Interscience: New York, 1983.

(72) Rivoal, J. C.; Briat, B. *Mol. Phys.* **1974**, *27*, 1081−1108.

(73) Gerstman, B. S.; Brill, A. S. *J. Chem. Phys.* **1985**, *82*, 1212−1230.

Table 4. Summary of the Cu_A $\sigma_g \rightarrow \sigma^*_u$ Excited-State Distortion Analysis

		ground-state vibrational normal coordinates		excited-state internal coordinate distortions (Δr_i(Å))		
int coord	ground-state geometry	ν_1, 125 cm^{-1}	ν_4, 340 cm^{-1}	ν_1, 125 cm^{-1}	ν_4, 340 cm^{-1}	$\sigma_g \rightarrow \sigma^*_u$ excited-state equilibrium geometry
Cu···Cu	2.43 Å	0.1347	0.1155	0.349	0.099	2.88 Å
Cu−S	2.29 Å	−0.0309	0.1110	−0.080	0.095	2.31 Å
Cu−S−Cu	69°					77°
S−Cu−S	110°					103°

remains comparable to those of blue copper proteins,[74] but the rotated nature of the Cu_A HOMO leads to more similar absorption intensities in the two allowed S → Cu CT transitions. This rotated HOMO arises from mixing of the σ^*_u (b_{3u}) and π_u (b_{2u}) D_{2h} MOs, allowed when the Cu_A symmetry is reduced to C_i (where σ^*_u and π_u have a_u symmetry), and this mixing increases as the energy gap between these two orbitals decreases.

(D) Cu_A $\psi-\psi^*$ Excited-State Distortion Analysis. The energy of band 3 measured spectroscopically (Figure 1) provides the magnitude of the electronic coupling matrix element responsible for the observed ground-state valence delocalization in Cu_A ($2H_{AB} \approx 13\,400$ cm^{-1}).[35] In addition to the magnitude of H_{AB}, information pertaining to the geometry dependence of H_{AB} may also be obtained from analysis of the $\psi \rightarrow \psi^*$ absorption bandshape and resonance Raman enhancement profiles that may then be used to evaluate the nuclear reorganization energy associated with reduction of this site.[56,57]

The resonance-enhanced Raman intensity of a vibrational peak at energy ν_n (cm^{-1}) is directly related to the magnitude of the excited-state nuclear displacement along the nth vibrational normal coordinate. The relative intensities of two modes, m and n, in a preresonance[75−77] or short time scale[78,79] Raman spectrum are related to the relative dimensionless coordinate displacements, Δ, using eq 1, and absolute scalings are estimated from the low-temperature absorption bandwidth using eq 2.

$$\frac{I_n}{I_m} \approx \frac{\Delta_n^2 \nu_n^2}{\Delta_m^2 \nu_m^2} \tag{1}$$

$$\text{fwhm} \approx [4 \ln 2(\sum_k \Delta_k^2 \nu_k^2)]^{1/2} \tag{2}$$

Laser excitation into band 3 leads to a Raman vibrational spectrum containing intensity primarily in four vibrational peaks (Figure 2), associated with the four normal coordinates depicted in Chart 2. The relative integrated intensities of these Raman peaks using excitation into band 3 of the wild-type Cu_A site from *B. subtilis* are 1.0 (125 cm^{-1}, ν_1):0.6 (258 cm^{-1}, ν_2):0.3 (272 cm^{-1}, ν_3):2.2 (340 cm^{-1}, ν_4). From eq 1, this gives relative dimensionless displacement parameters, $|\Delta^{rel}|$, of 1.0:0.4:0.3:0.5. Using eq 2 and a low-temperature fwhm value of ∼2100 cm^{-1} obtained from Gaussian resolution of the *B. subtilis* Cu_A absorption spectrum, these dimensionless displacement parameters yield scaled absolute value dimensionless displacement parameters, $|\Delta|$, of 5.0:1.9:1.3:2.7. To estimate the relative importance of each of these displacements in the total nuclear relaxation energetics, the excited-state vibrational relaxation energies, E_R, of each are compared. The E_R values are determined from eq 3, where $\Delta^2/2$ is identical to the Huang−Rhys harmonic displacement factor, S. This analysis gives

$$E_{R(n)} = \left(\frac{\Delta_n^2}{2}\right)\nu_n \tag{3}$$

vibrational relaxation energies of 1550, 450, 210, and 1260 cm^{-1} for these four distortions ($\nu_1-\nu_4$), which are respectively 45, 13, 6, and 36% of the total 3470-cm^{-1} excited-state vibrational relaxation energy. From this comparison, it is clear that the excited-state vibrational relaxation energy is dominated by the accordion (ν_1) and breathing (ν_4) coordinates in Chart 2, as these are similar in magnitude and together account for ∼80% of the total excited-state vibrational relaxation energy.

The geometric nature of the excited-state distortion may be determined by relation of the excited-state displacement parameters, Δ, along each normal coordinate to the geometric descriptions for these coordinates obtained from a vibrational normal coordinate analysis.[80−82] Specifically, the internal coordinate displacements, Δr_i (Å), are determined from the normal coordinate displacements using eq 4, where $l_{n,i}$ is the ith element of the mass-weighted eigenvector, L_n, for the nth normal mode.

$$\Delta r_i \text{ (Å)} = 5.8065 \sum_n l_{n,i}(\Delta_n/\sqrt{\nu_n}) \tag{4}$$

Approximating the excited-state distortion in Cu_A to have contributions only from the two dominant distortions, ν_1 and ν_4, the resulting excited-state internal coordinate distortions, Δr, for the four-atom core are presented in Table 4. The absolute phases of these two excited-state distortions are not determined directly from experiment. In this analysis, we note that the Cu−Cu $\sigma_g \rightarrow \sigma^*_u$ nature of this electronic transition will cause a greater Cu−Cu separation in the σ^*_u excited state than in the σ_g ground state,[56] and the phases leading to contraction of the Cu−Cu core in the σ^*_u excited state are, therefore, eliminated from consideration. The resulting excited-state equilibrium geometry is summarized in Table 4 and in Chart 3.

From Chart 3 and Table 4, it is seen that, in the σ^*_u excited state, the Cu−Cu separation increases, while there is very little change in Cu−S separation (Δr_{tot}(Cu−S) ≈ 0.02 Å). This results in displacement of the two Cu atoms away from the center of the core by ∼0.22 Å each and displacement of the S atoms *toward* the center of the core by ∼0.14 Å each. Thus, the net distortion of the Cu_2S_2 core upon $\sigma_g \rightarrow \sigma^*_u$ excitation

(74) Hay, M. T.; Ang, M. C.; Gamelin, D. R.; Solomon, E. I.; Antholine, W. T.; Blackburn, N. J.; Massey, P. D.; Kwon, A. H.; Lu, Y. *Inorg. Chem.* **1998**, *37*, 191−198.
(75) Warshel, A. *Annu. Rev. Biophys. Bioeng.* **1977**, *6*, 273−300.
(76) Warshel, A.; Dauber, P. *J. Chem. Phys.* **1977**, *66*, 5477−5488.
(77) Blazej, D. C.; Peticolas, W. L. *Proc. Natl. Acad. Sci. U.S.A.* **1977**, *74*, 2639−2643.
(78) Heller, E. J.; Sundberg, R. L.; Tannor, D. *J. Phys. Chem.* **1982**, *86*, 1822−1833.
(79) Heller, E. J. *Acc. Chem. Res.* **1981**, *14*, 368−375.
(80) Schachtschneider, J. H. Technical Report Nos. 231−264 and 57−65; Shell Development Co.: Emeryville, CA, 1964−1965.
(81) Wilson, E. B., Jr.; Decius, J. C.; Cross, P. C. *Molecular Vibrations*; Dover Publications: New York, 1980.
(82) A simplified normal coordinate analysis[80,81] was performed on a Cu_2S_2 rhomb. The modal descriptions obtained for the accordion and breathing modes (Table 4) are very similar to those previously published.[17]

Chart 3

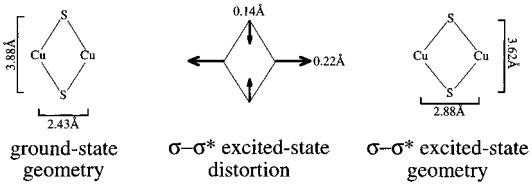

is a core bending motion that displaces the positions of all four atoms through changes in angles but does not involve significant changes in Cu−S bond lengths.

Discussion

In this section, we use the experimental band assignments and Xα-SW MO calculations to evaluate how differences in the ligand environments of Cu_A and the MV model may lead to their different electronic structures (Figures 7 and 9). Particular emphasis is placed on understanding the observed HOMO conversion from π_u in the MV structure to mostly σ^*_u in Cu_A. The electronic structure, valence delocalization, and redox properties of Cu_A are then evaluated in relation to its biological ET function.

Ligand-Field Control of Metal−Metal Bonding in the MV Model and Cu_A. Assignment of the Cu_A electronic transitions provides an understanding of specific aspects of its electronic structure and ligand coordination environment. Substantially more is learned by systematically comparing these properties with the analogous properties of the MV model. The structures of these two sites are similar in their three-coordinate pseudo-planar S_2N ligation around each Cu ion (Chart 1A,B). The major geometric perturbations of the MV model structure that would lead it to resemble the Cu_A structure are (a) core compression along the Cu−Cu axis (from 2.92 to ∼2.44 Å) and the concomitant S−Cu−S angle increase (from 100 to 116°), (b) weakening of the axial interactions (from 2.13 to >∼2.7 Å), and (c) compression of the Cu−N_{eq} bond length (from 2.15 to 1.95 Å). As described above, these two structures have significantly different HOMO character: Cu_A has a σ^*-type HOMO involving significant direct Cu−Cu interaction (Figure 9A), while the MV model has a π-type HOMO and no significant direct Cu−Cu interaction (Figure 7A). As is shown in the following section, the systematic correlation of the geometric and electronic structural differences between these two systems leads to an understanding of how the Cu ligand field may control the nature and magnitude of direct Cu−Cu bonding in such dimers.

Figure 10 quantitatively correlates the ligand-field MO splitting patterns of the MV model and Cu_A. Aside from the experimentally measured $\pi^*_g-\pi_u$ splitting (band 1), the exact magnitudes of the dimer splittings in the MV model (Figure 10, far left) are uncertain, since only transitions from the *gerade* doubly occupied orbitals to the *ungerade* π_u HOMO are observed. The energy splittings of the pairs of out-of-plane MV model orbitals are arbitrarily plotted as 1000 cm^{-1}, while the $\sigma_g-\sigma^*_u$ splitting is depicted as 8000 cm^{-1}. The situation is similar for Cu_A (Figure 10, far right): The energies of the five *gerade* orbitals relative to the HOMO are known from the spectral assignments, but additionally the energy of the π_u orbital is known from quantitative EPR simulations.[32] Thus, both the $\sigma_g-\sigma^*_u$ and $\pi^*_g-\pi_u$ dimer splittings in Cu_A are known experimentally. Averaging the dimer splittings for each orbital pair gives the MO diagrams for the hypothetical monomeric fragments associated with the MV model (Figure 10, left center) or Cu_A (Figure 10, right center).

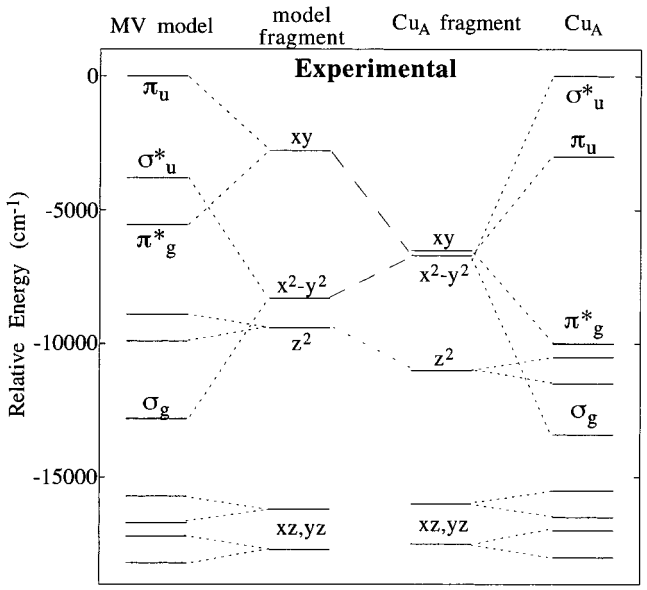

Figure 10. Experimental correlation diagram relating the molecular orbital splitting patterns of the mixed-valence (MV) model and Cu_A. (Far left) Experimental band assignments for the MV model. (Left center) Monomeric ligand-field splitting diagram extracted from experimental MV dimer splitting pattern. (Far right) Experimental band assignments for Cu_A. (Right center) Monomeric ligand-field splitting diagram for Cu_A extracted from experimental dimer splitting pattern. The exact magnitude of the $\sigma_g-\sigma^*_u$ splitting assumed for the MV model (Far left) alters the specific position of the x^2-y^2 parent orbital but does not affect the general trend of converging x^2-y^2 and xy parent orbital energies in Cu_A.

The monomeric splitting pattern of the MV model (Figure 10, left center) shows the *xy* orbital isolated at high energy, followed by the x^2-y^2 and z^2 orbitals, and then deepest in energy are the *xz,yz* orbitals. This pattern is characteristic of a C_{2v} ML_3 fragment when the unique angle is less than 120°. The presence of a Cu−N_{ax} bond in the MV model selectively raises the energy of the z^2 orbital to an energy comparable to that of the in-plane x^2-y^2 orbital (Figure 10, left center). Cu_A shows a different monomeric splitting pattern (Figure 10, right center), in which the x^2-y^2 orbital has moved up in energy, while the *xy* orbital has moved down in energy (relative to the *xz,yz* pair), as anticipated for its more trigonal-planar monomeric unit. In the limit of a trigonal field, the x^2-y^2 and *xy* monomeric d orbitals are degenerate, and, therefore, widening the S−Cu−S angle in Cu_A (S−Cu−S ≈ 116°) relative to that in the MV model (S−Cu−S ≈ 100°) is expected to bring these two parent orbitals closer in energy. The decreased energy of the z^2 orbital in Cu_A is consistent with the weakened axial interaction observed in X-ray crystallographic studies[14,16] and implied by EXAFS results.[12,13]

Dimer splittings most affect the two in-plane orbital pairs, $\sigma_g-\sigma^*_u$ and $\pi_u-\pi^*_g$ (Figure 10). The isolated nature of the *xy* parent orbital in the monomeric fragment of the MV complex results in an isolated π_u-type HOMO, with the lowest energy electronic transition being from its π^*_g counterpart, *i.e.*, the mixed-valence $\psi \rightarrow \psi^*$ transition. For Cu_A, however, the similar energies of the *xy* and x^2-y^2 parent orbitals allow the σ^*_u orbital, which splits more than the π_u orbital due to additional Cu−Cu σ-bonding interactions, to become the highest energy MO despite starting at slightly lower energy in the hypothetical monomeric fragment (Figure 10, right). The general trends are reproduced by Xα-SW calculations (*vide supra*), which in particular predict the convergence of the x^2-y^2

Scheme 1

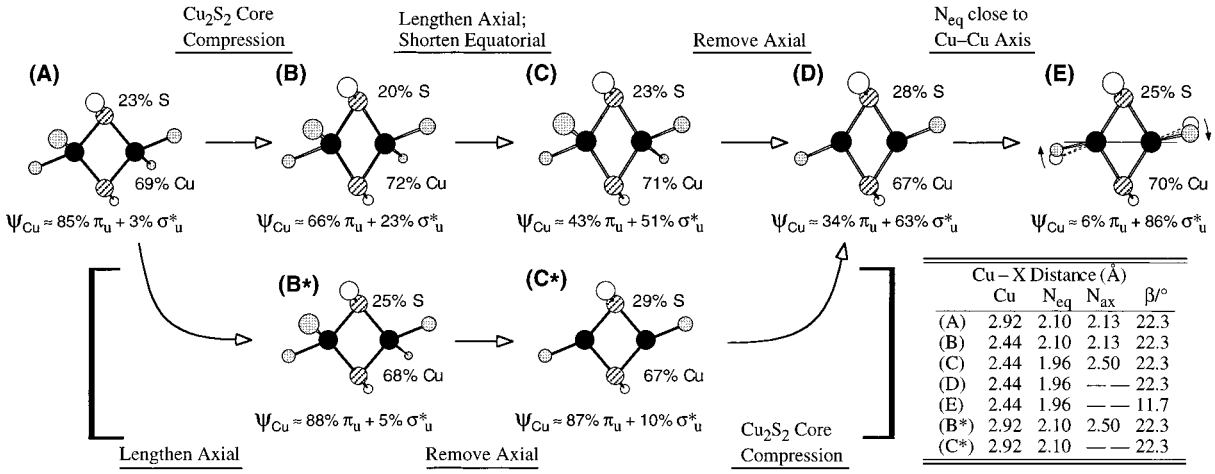

	Cu–X Distance (Å)			
	Cu	N_{eq}	N_{ax}	β/°
(A)	2.92	2.10	2.13	22.3
(B)	2.44	2.10	2.13	22.3
(C)	2.44	1.96	2.50	22.3
(D)	2.44	1.96	— —	22.3
(E)	2.44	1.96	— —	11.7
(B*)	2.92	2.10	2.50	22.3
(C*)	2.92	2.10	— —	22.3

and *xy* parent orbital energies in Cu_A relative to the MV model and also reproduce the stabilization of z^2 observed in Cu_A relative to the model.

In summary, comparison of the experimental orbital splitting patterns between the MV model and Cu_A (Figure 10, center) shows a series of orbital energy changes that are related directly to the structural changes between the sites and, in particular, reveal that the change in orbital ground state from π_u in the model geometry to σ^*_u in the Cu_A geometry is due to well-defined changes in the ligand-field environment (wider S−Cu−S angles and shorter Cu−Cu separation in Cu_A), which result in convergence of the *xy* and x^2-y^2 parent orbitals and an increase in dimer splittings.

Xα-SW Virtual Mutagenesis: Engineering a Hypothetical Cu_A Site. The MO analysis presented above (Tables 1 and 3, Figures 7, 9, and 10) suggests that one of the defining differences between the electronic structures of Cu_A and the MV model is the amount of Cu−Cu σ^*_u character in the HOMO: in the MV model, the Cu d character of the HOMO is dominantly π_u (85% π_u and 3% σ^*_u in the Xα-SW calculations, Figure 7A), while in Cu_A the Cu character of the HOMO is mostly σ^*_u (86% σ^*_u and 6% π_u in the C_i Xα-SW calculations, Figure 9A). In an effort to evaluate the relative contributions of the structural perturbations listed above to generation of the Cu_A σ^*_u HOMO, Xα-SW calculations were performed on a series of hypothetical dimer structures which systematically transform the MV model structure into a Cu_A center (Scheme 1, Table S4). Correlating the geometric perturbations with changes in the electronic structure allows the effect of each to be evaluated independently.

From these calculations, we learn that the most important structural perturbation in the hypothetical transformation of the MV model into a Cu_A center is the decreased Cu−Cu distance. This key perturbation alone does not complete the electronic structure transformation, however, and substantially weakened Cu−axial ligand interactions also play a critical role in the generation of the σ^*(HOMO) observed in the Cu_A center. Compressing the Cu−Cu distance imparts significant σ^* character (23%) to the HOMO (Scheme 1B), while weakening, and even removing, the axial ligand interaction without shortening the Cu−Cu separation leads to a limiting π_u:σ^*_u ratio of 87%:10% (Scheme 1B*,C*). Continuing the geometrical transformation by combining these perturbations effects the conversion to a dominantly σ^* HOMO (Scheme 1C,D). Therefore, both perturbations must occur in order to achieve the σ^* HOMO observed in Cu_A. Finally, the angular position of the N_{eq} ligand relative to the Cu−Cu axis (β) also affects the electronic structure substantially (Scheme 1E).[83] Within the group of Cu_A sites studied to date, small changes in the angular positions of the N_{eq} ligands and the strengths of the axial interactions are, therefore, expected to fine-tune the degree of π_u and σ^*_u mixing, giving rise to the varied spectral features observed in Figure 1.[84]

The protein environment can implement at least one of the critical perturbations in the Cu_A site, namely the weak axial interactions, by restricting the ability of the Glu and Met axial residues to approach the Cu ions. The ligand-field environment imposed on the Cu_A site by the protein would, therefore, be akin to the rack/entatic state discussed in reference to blue copper proteins, where a weak axial interaction is considered to be imposed by the protein matrix.[85] The contraction of the Cu−N_{eq} bonds observed in Cu_A is probably a consequence of charge compensation resulting from the reduced donor strength of the axial ligands, and it is likely that the contraction of the Cu−Cu separation also occurs in reaction to the removal of the axial ligands and the orbital change this allows (*i.e.*, the 45° rotation from π_u to σ^*_u, Scheme 2).[86]

Scheme 2

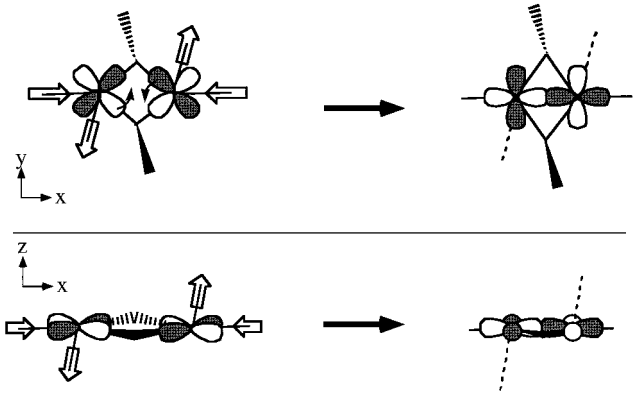

(83) Although some distribution in Cu_A Cu−S bond lengths is suggested in the EXAFS and crystal structures, introduction of a rhombic distortion in the C_i calculations via a 0.05-Å difference in adjacent Cu−S distances showed only minimal electronic structural effects (not shown). We also note that, between the limits explored in these calculations (1.95−2.15 Å), the strength of the Cu−N_{eq} interaction seems to have significantly less influence on the electronic structure than the Cu−Cu compression and weakened axial interaction. This suggests that the short Cu−N_{eq} distance observed in Cu_A is the result of charge compensation for the weakened axial interaction.

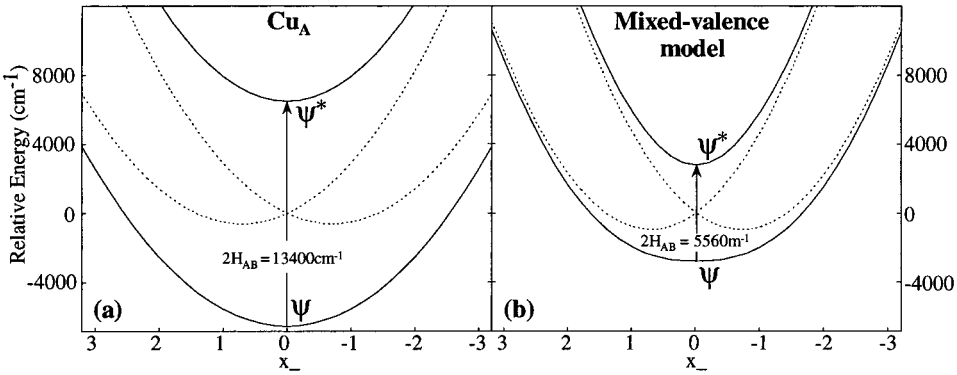

Figure 11. Q_- ground-state potential energy surfaces calculated for Cu_A (a) and the mixed-valence model (b) using eq 5. The specific parameters used are (a) $2H_{AB} = 13\,400$ cm^{-1}, $\lambda^2/k_- = 2450$ cm^{-1} (from $\nu_- = 250$ cm^{-1}, $\mu_- = 44$ g/mol (from average of 2S + imidazole (67 g)), $n = 3$, and $\Delta r = 0.1$ Å), and (b) $2H_{AB} = 5560$ cm^{-1}, $\lambda^2/k_- = 2190$ cm^{-1} (from $\nu_- = 280$ cm^{-1}, $\mu_- = 23$ (from average of 2S + 2N), $n = 4$, and $\Delta r = 0.1$ Å).

Delocalization and Cu−Cu Bonding. In this section, we evaluate the properties of Cu_A and the MV model that relate to their valence delocalization. Electron delocalization in mixed-valence dimers occurs when electronic coupling between the two ions overcomes vibronic trapping. The influence of each is generally described by eq 5,[87,88]

$$E^{\pm} = \frac{1}{2}\left(\frac{\lambda^2}{k_-}\right)x_-{}^2 \pm \left[\frac{1}{2}\left(\frac{\lambda^2}{k_-}\right)^2 x_-{}^2 + H_{AB}{}^2\right]^{1/2} \qquad (5)$$

where the vibronic trapping term, $(\lambda^2/k_-) \approx k_-(n^{1/2}\Delta r_{redox})^2$, $k_- = \pi^2 c^2 \mu_- \nu_-{}^2$, and H_{AB} is the electronic coupling matrix element regulating inter-ion electron transfer. The (−) subscripts on these terms refer to the symmetry-breaking nuclear coordinate comprised of the antisymmetric combination of monomeric (A, B) breathing motions, referred to as Q_- in the PKS model,[89] *i.e.*, $Q_- = 2^{-1/2}(Q_A - Q_B)$, k_- is the nuclear force constant associated with distortion along Q_- (in cm^{-1}/Å^2), μ_- is the Q_- modal mass (in g/mol), and ν_- is the Q_- vibrational frequency (in cm^{-1}). The experimentally determined $2H_{AB}$ ($=E_{\psi-\psi^*}$, see refs 35, 56, and 57) values are 5560 cm^{-1} in the MV model and ∼13 400 cm^{-1} in Cu_A. Whereas the MV model and the Cu_A sites are both valence delocalized, they have different HOMOs, and, consequently, their pathways for delocalization are different. Because of the large Cu−Cu separation, delocalization in the MV model must occur *via* the two bridging thiolates in a superexchange-type pathway (Figure 7A). In Cu_A, however, the delocalization pathway has a superexchange-type contribution comparable to that in the MV model, but it additionally has a sizable direct Cu−Cu $\sigma_g - \sigma^*_u$ contribution (Figure 9A).

The specific ground- and excited-state potential surfaces relevant to valence delocalization in these two dimers may be calculated from eq 5 using experimental $2H_{AB}$ values obtained from the $\psi \rightarrow \psi^*$ transition energies[35,56,57] and $\lambda^2/2k_-$ values estimated from vibrational energies and literature values for redox-induced bond length changes (Figure 11). These surfaces illustrate that the delocalized ground state of Cu_A (Figure 11a, solid) is extremely stabilized beyond what is necessary to overcome its inherent vibronic trapping energies (Figure 11a, dashed). The surfaces calculated for the MV model also show a delocalized ground state (Figure 11b, solid), but this delocalization is not as stabilized relative to its inherent trapping energies (Figure 11b, dashed) as that in Cu_A, due predominantly to the smaller $2H_{AB}$. The significantly enhanced electronic coupling in Cu_A can be directly associated with the direct Cu−Cu $\sigma_g - \sigma^*_u$ contribution of ∼7800 cm^{-1} that is absent in the MV model. When compared to literature $\sigma - \sigma^*$ transition energies observed in first-row transition-metal dimers having unsupported metal−metal bonds ($E_{\sigma-\sigma^*} > \sim 24\,000$ cm^{-1}),[90] this interaction in Cu_A is seen to be relatively weak, corresponding to a bond order of only $\sim^1/_2 - ^1/_4$. The maximum bond order attainable in a one-hole system such as this is $^1/_2$. Nevertheless, the large contribution to valence delocalization from this direct Cu−Cu bonding does play a significant and perhaps critical role in the electronic structure of the Cu_A site by allowing Cu_A to remain delocalized despite its low-symmetry protein environment.[84,91]

In summary, the Cu−Cu σ^*_u ground state of Cu_A and the π_u ground state of the MV model are interconvertible *via* a well-defined set of ligand-field perturbations at the copper ions. These ligand-field perturbations are responsible for the presence of a Cu−Cu σ-bonding interaction in Cu_A, which is, in turn, responsible for the extreme stabilization of the delocalized ground state in Cu_A (Figure 11).

(84) The absorption, MCD, and EPR spectra of the MV model bear many striking similarities to those of the Cu_A-type site in PCyoA[34] (see Figure 3 and Supporting Information). This strongly suggests that PCyoA has a π_u HOMO rather than the predominantly σ^*_u HOMOs typical of wild-type Cu_A sites, and that this HOMO is fully delocalized in PCyoA as in the MV model.

(85) Guckert, J. A.; Lowery, M. D.; Solomon, E. I. *J. Am. Chem. Soc.* **1995**, *117*, 2817−2844.

(86) The possibility that the Cu−Cu separation decreases as a result of a protein-forced S−S elongation is considered less likely since the sharp angles of the cysteine carbons out of the Cu_2S_2 plane should allow some flexibility in the positions of the S(Cys) atoms.

(87) Blondin, G.; Girerd, J.-J. *Chem. Rev.* **1990**, *90*, 1359−1376.

(88) Girerd, J.-J. *J. Chem. Phys.* **1983**, *79*, 1766−1775.

(89) Piepho, S. B.; Krausz, E. R.; Schatz, P. N. *J. Am. Chem. Soc.* **1978**, *100*, 2996−3005.

(90) Abrahamson, H. B.; Frazier, C. C.; Ginley, D. S.; Gray, H. B.; Lilienthal, J.; Tyler, D. R.; Wrighton, M. S. *Inorg. Chem.* **1977**, *16*, 1554−1556.

(91) The inequivalent axial ligation of the two coppers in Cu_A requires consideration of the effect of asymmetry on the potential surfaces shown in Figure 11a. Inequivalent potentials of the two coppers are introduced into eq 5 by substitution of $(\lambda^2/k_-)x_- \rightarrow (\lambda^2/k_-)x_- + W$, where $\Delta E = \sqrt{2}W$ is the potential difference between the two halves of the dimer. (Wong, K. Y.; Schatz, P. N. *Prog. Inorg. Chem.* **1981**, *28*, 369−449.) The asymmetric ground-state surface that results from $\Delta E \neq 0$ affects localization by skewing the potential surface (even a single-minimum surface) such that more electron density is located on one side than the other. Including this substitution in eq 5 and using the parameters of Figure 11a reveals that a potential difference of 150 mV between the two Cu ions in Cu_A results in only ∼10% charge localization toward one copper, while the same potential inequivalence results in ∼28% localization in the MV model. The minor effect of ΔE in Cu_A is due to the very large value of H_{AB}. Thus, to observe significant valence trapping in Cu_A, either the potential difference between the two coppers must be very large ($\Delta E > \sim 150$ mV) or the electronic coupling pathway must be disrupted and H_{AB} diminished.

Functional Relevance of Cu_A Dimeric Structure, Cu−Cu Bonding, and Valence Delocalization. Weak axial interactions imposed by the protein and the compression of the Cu_2S_2 core along the Cu−Cu axis impart the Cu_A center with an unusual valence-delocalized electronic structure, which will affect the biological ET function of the site. The rate of ET is dependent upon three basic factors, as described by eq 6:[92−94]

$$k_{ET} = \sqrt{4\pi^3/h^2\lambda kT}(H_{DA})^2 \exp[-(\Delta G°+\lambda)^2/4\lambda kT] \quad (6)$$

the donor−acceptor electronic coupling (H_{DA}), the vibronic or Franck−Condon reorganization energy associated with the ET redox chemistry (λ), and the difference in redox potentials, or driving force, between the donor and acceptor sites involved in each ET step ($\Delta G°$).

Here we evaluate the properties of Cu_A contributing to each of these three terms and relate them to the analogous properties of blue copper centers in an attempt to assess the role of the Cu_A dimeric structure, Cu−Cu bonding, and valence delocalization in promoting efficient ET.

(A) H_{DA}. We have previously reported[35] that the large Cu−S(Cys) covalency of the Cu_A site (∼13% per S(Cys)) biases the ET process toward a pathway *via* the cysteine residues relative to the histidine residues, for which the covalent interaction with the Cu ion is only ∼1−3% per N(His). This anisotropic covalency leads to a weighting factor of ∼19−169 in the relative rates k_{ET}(S(Cys))/k_{ET}(N(His)). Inspection of the newly available protein crystallographic coordinates for bovine heart C*c*O[15,16,50,51] reveals that this anisotropic covalency, therefore, introduces a second ET pathway (pathway 2, proceeding *via* C196) that is competitive with that previously considered[65] (pathway 1, proceeding *via* H204). These two pathways are shown in Figure 12. Pathway 1 involves 12 covalent and two hydrogen-bonding interactions, excluding the two metal−ligand bonds. Pathway 2 involves 22 covalent and two hydrogen-bonding interactions, excluding the two metal−ligand bonds. Since the acceptor site in each case is the same, this Fe−N covalency does not affect the comparison of these pathways. Using standard pathway estimates[92] and eq 6, the predicted ratio k_{ET}(path 2)/k_{ET}(path 1) ≈ 1.02−0.11. A larger ratio would result if the 0.6-Å shorter first hydrogen-bonding interaction in pathway 2 (O−O ≈ 2.76 Å) compared to that in pathway 1 (O−N ≈ 3.36 Å) were taken into account.[92] Finally, this ratio is also sensitive to the specific number used for the N(His) covalency. ENDOR[28] and paramagnetic NMR[95] studies demonstrate two inequivalent N(His) covalencies in the Cu_A HOMO. The paramagnetic NMR results[30] and CNDO calculations including the full histidine rings[33] suggest that the N(His) involved in ET pathway 1 (H204) is the less covalent N(His), which would suggest that the upper limit for the ratio (*i.e.*, k_{ET}(path 2)/k_{ET}(path 1) ≈ 1.02) would be expected. In summary, the rate constants for these two Cu_A → heme *a* ET pathways can be comparable despite ∼10 additional covalent bonds in pathway 2 due to the high covalency of the Cu−S bonding interaction in Cu_A.

While much attention has been given to the specifics of ET between Cu_A and heme *a*, the ET process between cytochrome *c* and Cu_A remains poorly defined. Cytochrome *c* is believed to dock in an acidic patch of the membrane surface ∼9 Å from the Cu_A site.[14] This distance is substantially greater than the analogous docking site distance in plastocyanin (∼4.5 Å), and inspection of the bovine heart C*c*O structure[15,16] shows that the proximal histidine ligand of Cu_A (H161) is shielded from the surface, precluding direct overlap with the cytochrome. These observations suggest that cytochrome *c* → Cu_A ET follows a protein-based pathway, and it has been proposed[14] that the nearby tryptophan residue (W104) might be involved, as this protrudes from the protein surface in the vicinity of the proposed cytochrome docking site. The bovine heart C*c*O structure shows a hydrogen-bonding interaction between N(W104) and the carbonyl oxygen of C200 (N−O ≈ 3.15 Å, Figure 12). This oxygen is only four covalent bond lengths removed from the S(C196) in the Cu_A site and would, therefore, provide an efficient ET pathway between these two sites.[96] The observation that one S(Cys) (C200) is linked favorably for cytochrome *c* → Cu_A ET while the other (C196) is competitive with H204 for Cu_A → heme *a* ET suggests that a possible function of the dithiolate portion of the Cu_A structure is to provide pathways for both interprotein ET into Cu_A and intraprotein ET out of Cu_A. This difference between Cu_A and blue copper could arise from the fact that the Cu_A site in C*c*O is buried deeper in the protein matrix than are blue sites, which are generally located at the surface.

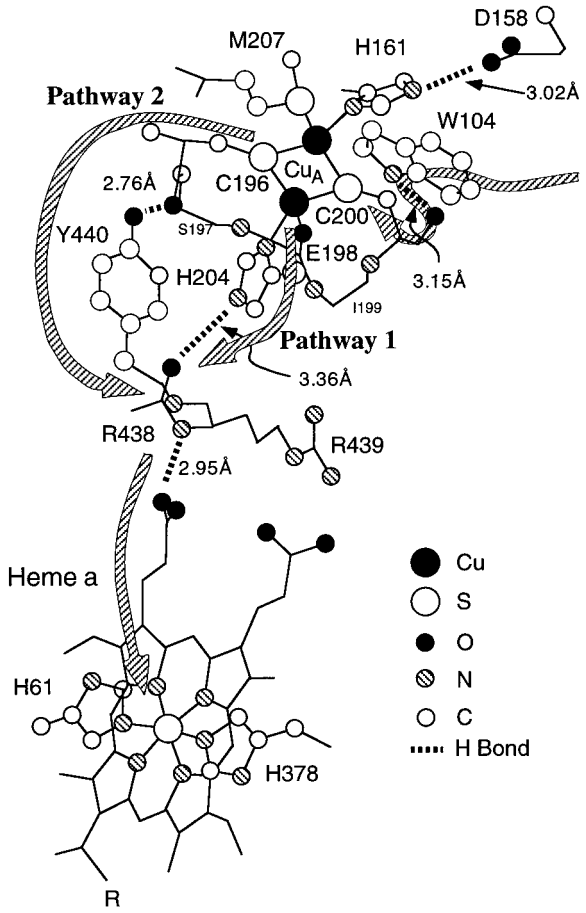

Figure 12. Proposed ET pathways in bovine heart C*c*O based on comparative rate calculations. The two Cu_A → heme *a* pathways shown are predicted to be competitive in rate, while the cytochrome *c* → Cu_A (via W104) pathway shown is expected to dominate.[96]

(92) Beratan, J. N.; Betts, J. N.; Onuchic, J. N. *Science* **1991**, *252*, 1285−1288.

(93) Marcus, R. A.; Sutin, N. *Biochim. Biophys. Acta* **1985**, *811*, 265−322.

(94) Newton, M. D. *Chem. Rev.* **1991**, *91*, 767−792.

(95) Dennison, C.; Berg, A.; de Vries, S.; Canters, G. W. *FEBS Lett.* **1996**, *394*, 340−344.

(96) The ∼6-fold greater covalency of S(Cys) relative to N(His) gives the W104/C200 path a ∼13-fold overall advantage over a D158/H161 path, assuming equal ET rates from cytochrome *c* to D158 or W104.

(B) Franck−Condon Barrier to ET. The vibronic, or Franck−Condon, barrier for protein ET reactions (λ in eq 6) is typically in the range from ∼5000 to 10 000 cm^{-1}. This barrier has been determined experimentally for Cu_A → heme *a* ET to be extremely small (∼2400 cm^{-1}).[65,97] The specific properties of Cu_A nuclear reorganization during ET may be estimated using the vibronic properties of the Cu−Cu $\psi \rightarrow \psi^*$ electronic transition by recognizing that the orbital description of the $\psi \rightarrow \psi^*$ electronic transition, $(\sigma_g)^2(\sigma^*_u)^1 \rightarrow (\sigma_g)^1(\sigma^*_u)^2$, is related to that of the Cu_A biological redox cycling, $(\sigma_g)^2(\sigma^*_u)^1 \leftrightarrow (\sigma_g)^2(\sigma^*_u)^2$, where the difference is formally one electron in the σ_g MO. If the stabilization energy gained from one electron in the σ_g MO is approximately equal to the destabilization energy contributed by one electron in the σ^*_u MO, then the $\psi \rightarrow \psi^*$ excited-state reorganization energy is approximately twice that of the nuclear reorganization energy associated with one-electron reduction of the site. This approximation neglects the net change in charge of the site, which would add an additional energy associated with the expansion of all metal−ligand bonds. Using this approximation, the nuclear reorganization energy upon reduction of the mixed-valence *B. subtilis* Cu_A site is estimated to be ∼1750 cm^{-1}, associated largely with a Cu−Cu elongation of ∼0.22 Å (Chart 3). Recent EXAFS studies on *B. subtilis* and *T. thermophilus* Cu_A sites[13] show similar core bending distortions ($\Delta r_{Cu-Cu}(av) \approx 0.08$ Å) upon reduction. The low energy associated with this Cu_2S_2 core bending distortion thus provides a small Franck−Condon barrier to ET.

Blue copper ET sites have very small nuclear reorganization energies associated with redox changes,[85] typically in the range of ∼3200 cm^{-1}. The smaller reorganization energy of only ∼2000 cm^{-1} in Cu_A is attributable to its dimeric structure, both in the geometric sense and in the electronic sense (*i.e.*, the delocalized, mixed-valence oxidation state); distribution of nuclear reorganization over a dimer reduces both the inner- and outer-sphere nuclear reorganization energies. An estimate of the inner-sphere reorganization energy is provided by eq 7,

$$E_{R(i)} \approx k_{dis} n (\Delta r)^2 \qquad (7)$$

where k_{dis} is the force constant of the effective distortion coordinate, n is the number of distorting metal−ligand bonds, and Δr_{redox} is the magnitude of metal−ligand bond distortion upon redox change.

In the general case, a monomeric Cu(II) ion (or a valence trapped Cu(I)Cu(II) dimer) will have half as many metal−ligand bonds distorting upon reduction as a Cu(1.5)Cu(1.5) delocalized mixed-valence dimer: *i.e.*, $n_{mon}/n_{dim} = 0.5$. Alternatively, the magnitude of the bond length change in the monomeric site will be approximately twice as large as in the Cu(1.5)Cu(1.5) dimer: *i.e.*, $\Delta r_{mon}/\Delta r_{dim} \approx 2$. Using eq 7 with these values and assuming approximately equivalent internuclear force constants, k_{dis}, indicates that the ratio of monomer to delocalized dimer inner-sphere reorganization energies should be on the order of $E_{R(mon)}/E_{R(dim)} \approx 2$.[36,98] In addition to this *a priori* factor of 2 arising from two-center delocalization in Cu_A, however, the sizable reduction in Cu_A vibrational energies (∼100−350 cm^{-1}) relative to those in blue copper systems (∼250−500 cm^{-1})[23] suggests a corresponding decrease in k_{dis} in eq 7, associated with the reduced force constants of bridging *vs* terminal ligation. Finally, there is evidence to suggest that charge delocalization in Cu_A may also reduce the local outer-sphere reorganization energetics associated with ET, although the macroscopic electrostatic reorganization associated with long-range ET will not be altered: recent studies of solvational barriers to ET in systems involving charge-delocalized acceptor sites show an exponential increase in k_{ET} with increasing charge radius.[99] Thus, any local solvent reorganization in the immediate vicinity of Cu_A will be diminished relative to a monomer by charge delocalization over the dimer.

In summary, both the inner- and outer-sphere reorganization energies associated with ET redox chemistry may be reduced in Cu_A relative to blue copper centers due to electronic delocalization in the mixed-valence oxidized state of Cu_A. It is generally agreed, however, that the Franck−Condon barrier to ET in blue copper systems is already extremely small in the context of the entire ET process, and this factor is, therefore, probably not the dominant functional role of valence delocalization in Cu_A.

(C) Redox Potential. Reduction potentials of oxidized Cu_A sites are ∼+250 mV,[2,39,62,63] within the range observed in blue copper proteins but well above that of the MV model (∼−280 mV *vs* NHE, irreversible).[42] It is well known from blue copper and model studies that highly covalent copper thiolate bonding stabilizes the oxidized Cu^{2+} oxidation state. In blue copper, this effect is counterbalanced by the removal of the axial donor ligand, which has the effect of driving the reduction potential more positive (Table 2). A similar scenario may be described for Cu_A, where covalent copper thiolate bonding lowers the reduction potential, while the removal of the axial ligands raises it back into a range suitable for ET function (Table 2). The presence of not one but two cysteine ligands, however, suggests that the value of +250 mV is higher than would be anticipated and that charge delocalization may also contribute significantly to tuning this potential: delocalization between the two copper ions is expected to raise the reduction potential relative to a dithiolate-bound Cu^{2+} monomer or trapped mixed-valence dimer by inclusion of an additional positively charged ion in the HOMO wavefunction (*e.g.*, $[Cu(SR)_2]^0$ *vs* $[Cu_2(SR)_2]^+$), thereby dissipating the negative donor character of the bridging thiolates. Thus, a major role of valence delocalization in mixed-valence Cu_A may, in fact, be its relation to redox tuning of the site for effective ET while still allowing for the presence of two Cu−cysteine ET pathways, one into and the other out of the Cu_A center.

Summary

Consideration of the three factors influencing ET rates in biological systems suggests that there is a functional advantage to having two highly covalent copper−cysteine bonds, namely to enhance ET into and out of the buried Cu_A site. The presence of two coordinated anionic cysteine thiolates in a monomeric Cu complex, however, would severely impair the ET process by stabilizing the oxidized Cu^{2+} state and driving the reduction potential too negative. In Cu_A this is averted by weakened axial bonding interactions, as in blue copper systems, and by charge delocalization over two Cu ions. Charge delocalization in Cu_A is greatly facilitated by the very short, 2.44-Å Cu−Cu separation, since the direct Cu−Cu $\sigma-\sigma^*$ bonding interaction at this distance contributes at least as much to the Cu_A inter-ion electronic coupling matrix element, H_{AB}, as does the superexchange pathway through the thiolate bridges. This short Cu−Cu separation and $\sigma-\sigma^*$ bonding interaction in Cu_A may be regulated by the protein through elongation of the Cu axial bonds and the accompanying orbital rotation.

Acknowledgment. The authors thank Dr. L. B. LaCroix for assistance with Xα-SW calculations and M. Ang for assistance

(97) Brzezinski, P. *Biochemistry* **1996**, *35*, 5611−5615.
(98) Bominaar, E. L.; Achim, C.; Borshch, S. A.; Girerd, J. J.; Münck, E. *Inorg. Chem.* **1997**, *36*, 3689−3701.
(99) Hupp, J. T.; Zhang, X. L. *J. Phys. Chem.* **1995**, *99*, 853−855.

with azurin Cu_A preparation. This work was supported by funding from the NSF (Grant CHE9528250 to E.I.S., CAREER Award CHE9502421 to Y.L., and National Young Investigator Award to W.B.T.), the NIH (GM47365 to W.B.T. and GM18812to D.W.R.), and The Netherlands Organization of Research (NWO, to S.V.). D.R.G. thanks the Veatch Foundation for financial support.

Note Added in Proof: The proposed ET pathways involving the Cu_A site are further supported by the presence of analogous pathways in the recently released PDB file for *P. denitrificans* CcO (PDB code: 1ar1). Recent site-directed mutagenesis experiments (Witt, H.; Malatesta, F.; Nicoletti, F.; Brunori, M.; Ludwig, B. *J. Biol. Chem.* **1998**, *273*, 5132−5136) strongly support the proposed Trp → Cu_A pathway.

Supporting Information Available: Absorption, MCD, and EPR spectra comparing the MV model and PCyoA, SCF-Xα-SW calculated contours and results of the C_1 Cu_A calculation using the coordinates of bovine CcO (PDB code: 1occ), and tables reporting input parameters for SCF-Xα-SW calculations (15 pages, print/PDF). See any current masthead page for ordering information and Web access instructions.

JA973161K